Available online at www.sciencedirect.com

ScienceDirect

Geochimica et Cosmochimica Acta 168 (2015) 151–171

Geochimica et Cosmochimica Acta

www.elsevier.com/locate/gca

Ru isotope heterogeneity in the solar protoplanetary disk

Mario Fischer-Gödde [a,*], Christoph Burkhardt [a,b], Thomas S. Kruijer [a], Thorsten Kleine [a]

[a] *Institut für Planetologie, Westfälische Wilhelms – Universität Münster, Wilhelm-Klemm-Str. 10, 48149 Münster, Germany*
[b] *Origins Laboratory, Department of Geophysical Sciences, The University of Chicago, IL 60637, USA*

Received 11 November 2014; accepted in revised form 21 July 2015; available online 29 July 2015

Abstract

Nucleosynthetic isotope anomalies in bulk chondrites and differentiated meteorites reflect variable proportions of isotopically diverse presolar components in bulk planetary bodies, but the origin of these heterogeneities is not well understood. Here, the Ru isotope composition of a comprehensive suite of iron meteorites and bulk samples of ordinary, enstatite and carbonaceous chondrites, as well as acid leachates and an insoluble residue of the Allende chondrite are examined using newly developed multi-collector inductively coupled plasma mass spectrometry techniques. Except for IAB iron meteorites and enstatite chondrites, all investigated meteorites show well-resolved Ru isotope anomalies. Of these, within-group Ru isotopic variations observed for samples from a given chemical group of iron meteorites reflect secondary neutron capture induced Ru isotope shifts during prolonged cosmic ray-exposure. After correction of these cosmogenic effects using Pt isotopes as a neutron-dose monitor, the remaining Ru isotope anomalies are nucleosynthetic in nature and are consistent with a deficit in *s*-process Ru in iron meteorite parent bodies. Similarly, Ru isotope anomalies in bulk ordinary and carbonaceous chondrites also reflect a deficiency in *s*-process Ru. The sequential dissolution of Allende reveals the presence of an HF-soluble *s*-process carrier, which is either an unidentified presolar phase or a component that incorporated *s*-process Ru liberated from SiC grains during nebular or parent body processes. We show that varying proportions of the *s*-process carrier identified in Allende resulted in the correlated Ru isotope anomalies observed for bulk meteorites, and that all meteorites (except possibly IAB irons and enstatite chondrites) are depleted in this *s*-process component relative to Ru from the Earth's mantle. Bulk meteorites exhibit correlated Ru and Mo isotope anomalies, reflecting variable deficits of a common *s*-process component, but some iron meteorites and carbonaceous chondrites appear to deviate from this correlation. This may reflect unaccounted cosmic effects on Mo isotopes in iron meteorites, sample heterogeneities in carbonaceous chondrites or nebular and parent body processes acting differently on presolar Mo and Ru components.

The identification of *s*-deficits in Ru isotopes in almost all iron meteorites and chondrites investigated so far implies that meteorites do not seem to represent the material delivered to the Earth's mantle as a late veneer after cessation of core formation. However, additional analyses of a more comprehensive set of chondrites are necessary to firmly arrive at this conclusion.

1. INTRODUCTION

The presence of nucleosynthetic isotope anomalies in bulk meteorites indicates that varying proportions of isotopically diverse presolar components have been incorporated into early-formed planetary bodies. A variety of

* Corresponding author.
E-mail address: m.fischer-goedde@uni-muenster.de (M. Fischer-Gödde).

http://dx.doi.org/10.1016/j.gca.2015.07.032
0016-7037/

processes have been proposed to account for this planetary-scale isotopic heterogeneity. For instance, the isotope anomalies could reflect an initial heterogeneity in the distribution of presolar carrier phases in the early solar nebula, which may have arisen through the incomplete admixture of material injected from a nearby supernova (Trinquier et al., 2007; Dauphas et al., 2010; Qin et al., 2011; Steele et al., 2011). Varying proportions of Ca-Al-rich inclusions (CAI)—most of which are characterized by excesses or depletions in *r*-process nuclides (Brennecka et al., 2013)—among primitive meteorites (Leya et al., 2008; Akram et al., 2015) and the sorting of isotopically distinct dust grains according to their size or type (Regelous et al., 2008; Dauphas et al., 2010) may have also played a role. Some isotope anomalies in bulk meteorites may also be the result of nebular processes that led to unmixing of presolar components from an isotopically homogeneous dust reservoir (Trinquier et al., 2009; Burkhardt et al., 2012a). Thus, understanding the origin of the isotopic anomalies in bulk materials may help to constrain the efficiency of mixing in the early solar system and to assess the nebular processes affecting solid material contributing to the formation of planetesimals and planets. As such the isotopic anomalies in bulk meteorites may also be used to infer genetic relationships among different meteorites and between meteorites and the Earth (Dauphas et al., 2002a; Regelous et al., 2008; Burkhardt et al., 2011).

Iron meteorites and some chondrites display correlated Ru and Mo isotope anomalies consistent with the expected variations for the heterogeneous distribution of a presolar *s*-process carrier in the solar protoplanetary disk (Dauphas et al., 2004; Chen et al., 2010; Burkhardt et al., 2011). However, for some other elements such as Os, *s*-process matter seems to be homogeneously distributed among meteorites and the Earth (Brandon et al., 2005; Yokoyama et al., 2007, 2010; Walker, 2012). Of note, acid leachates and residues of primitive chondrites show large internal Os isotope variations (Reisberg et al., 2009; Yokoyama et al., 2010), and so the uniform and terrestrial Os isotope composition observed for meteorites indicates efficient mixing and homogenization of the distinct carriers of *s*- and *r*-process Os nuclides. Furthermore, the co-variation of Mo and W isotope anomalies in acid leachates and residues of the primitive chondrite Murchison suggest that bulk meteorites, given their large Mo isotope anomalies (Burkhardt et al., 2011), should also show significant nucleosynthetic W isotope anomalies (Burkhardt et al., 2012a,b). This is not observed, however, and bulk meteorites are characterized by only small if any nucleosynthetic W isotope anomalies (e.g., Qin et al., 2008; Kruijer et al., 2012). This observation led Burkhardt et al. (2012a) to suggest that thermal processing of presolar dust grains resulted in the release and partial loss of *s*-process Mo, causing the observed *s*-deficit in bulk meteorites, while W (and Os) were not or only slightly affected. The conditions under which such processing would have occurred, which meteorite groups were most affected, and how this thermal processing would have affected the combined Ru and Mo isotope systematics is unclear, however.

To address these issues and elucidate the dominant processes responsible for the generation of nucleosynthetic isotope anomalies in bulk meteorites, the study of Ru isotopes in meteorites is useful. Ruthenium has seven stable isotopes, with two isotopes produced via the *p*-process (^{96}Ru, ^{98}Ru), one produced in the *s*-process (^{100}Ru), one in the *r*-process (^{104}Ru), and three produced by both the *s*- and *r*-processes (^{99}Ru, ^{101}Ru and ^{102}Ru). These diverse nucleosynthetic origins of distinct Ru isotopes permit unequivocal identification and discrimination of *p*-, *r*-, and *s*-process anomalies, which is important for assessing the nature of the presolar component(s) causing isotope anomalies at the bulk meteorite scale. Chen et al. (2010) reported the first clear evidence for nucleosynthetic Ru isotope anomalies in bulk meteorites, which seem to be abundant particularly in iron meteorites. In this study, we developed new techniques for precise Ru isotope analyses by multi-collector inductively coupled plasma mass spectrometry (MC-ICPMS) and measured Ru isotopes in a comprehensive suite of iron meteorites and chondrites, as well as acid leachates and an insoluble residue from the Allende CV3 chondrite. We use these data to identify some of the nucleosynthetic Ru isotope components present in primitive meteorites and to assess whether any of these components is heterogeneously distributed at the bulk meteorite scale. We also assess whether all the Ru isotope anomalies are attributable to nucleosynthetic heterogeneities at the bulk meteorite scale or if some also reflect secondary modifications, such as cosmic ray-induced effects in iron meteorites or incomplete digestion of presolar grains in primitive chondrites (Brandon et al., 2005; Yokoyama et al., 2007). Finally, as a highly siderophile element, the bulk Ru in the Earth's mantle is generally thought to derive from the late veneer of primitive material added to the mantle after core formation was complete (e.g., Kimura et al., 1974; Chou, 1978). The comparison of the Ru isotope compositions of meteorites to that of the Earth might, therefore, place important constraints on the origin of the material constituting the late veneer.

2. SAMPLES AND ANALYTICAL METHODS

A total of 29 iron meteorites, covering the major iron groups (IAB, IIAB, IID, IIIAB, IVA, IVB), five ordinary chondrites, two enstatite chondrites, three carbonaceous chondrites (Allende, Gujba, Murchison), the primitive achondrite Tafassasset, and a terrestrial chromitite from the Shetland Ophiolite Complex in Scotland were analyzed for this study. Moreover, the Ru isotope compositions of five acid leachates and one acid insoluble residue from the Allende CV3 chondrite were analyzed. To assess the accuracy and reproducibility of the Ru isotope measurements, we also analyzed several aliquots of the NIST SRM 129c and 361 steels, the UB-N peridotite and two terrestrial basalt standards (BCR-2, BHVO-2), all doped with Ru from an Alfa Aesar standard solution. The amount of doped Ru added to the standard materials was adjusted to match the sample weights and Ru concentrations of the analyzed meteorites.

2.1. Sample preparation and decomposition

Iron meteorite samples (0.05–0.5 g) were received as small chips or were cut from larger pieces. Care was taken to exclude all obviously weathered material as well as fusion crust. For Gujba individual metal chondrules were removed by handpicking from a disaggregated sample and for Tafassasset a metal fraction was obtained from a grain size separate using a handmagnet. The metal surfaces of the iron meteorites and the Gujba samples were cleaned using abrasive paper and ethanol followed by leaching in 6 M HCl at 70 °C for 15 min on a hotplate. Iron meteorite and chondrite metal samples, as well as the NIST 129c and 361 samples, were digested in Savillex beakers using a 2:1 mixture of concentrated HNO_3 and concentrated HCl (reverse *aqua regia*) at 130 °C for 12 h on a hot plate.

The chondrite samples were received as powders or as chips free of visible saw marks. The chondrite chips were carefully cleaned by ultrasonication in distilled water and powdered in an agate mortar used exclusively for preparation of meteorites. The amount of sample used to prepare the chondrite powders was 2–4 g for Allende A, ordinary and enstatite chondrites, ~100 g for Allende MS-A, and ~1 g for Murchison. The chondrite powders (0.4–0.6 g) as well as doped powders of terrestrial rock standards (UB-N, BCR-2, BHVO-2) were digested in reverse *aqua regia* inside Carius tubes (CT) at 230 °C for 48 h (Shirey and Walker, 1995). Five samples of Allende and one of Murchison (and two doped UB-N samples) were dissolved using an alkaline fusion (AF) technique, whereby ~0.5 g of sample powder was fluxed with ~4 g of NaOH and ~2 g of Na_2O_2 in a furnace at sequentially increasing temperatures from ~325 to ~625 °C (Morgan and Walker, 1989). After cooling in a desiccator over night, the digestion cake was dissolved in Milli-Q H_2O and directly transferred to a Savillex PFA distillation unit (see below).

In addition, ~4 g of a homogeneous powder of the Allende chondrite (MS-A) were treated with the following sequential leaching procedure, which was adapted from Reisberg et al. (2009):

L1: 50 ml acetic acid + 50 ml H_2O, 1 day, 20 °C;
L2: 25 ml HNO_3 + 50 ml H_2O, 5 days, 20 °C;
L3: 30 ml HCl + 35 ml H_2O, 1 day, 75 °C;
L4: 30 ml HF + 15 ml HCl + 15 ml H_2O, 1 day, 75 °C;
L5: 10 ml HF + 10 ml HCl, 3 days, 150 °C;
L6: insoluble residue.

About half of each solution from leach steps L1-L5 was transferred to a Savillex PFA distillation unit for the purification of Ru (see below). An aliquot of the acid insoluble residue was digested using an alkaline fusion technique as described above.

2.2. Ion exchange chromatography and distillation of Ru

For the separation of Ru from the sample matrix two different techniques were employed. For samples digested in *aqua regia*, both inside Savillex vials or Carius tubes, Ru together with other highly siderophile elements (HSEs) was first separated by cation exchange chromatography followed by further purification and separation of the Ru from other HSEs through micro-distillation. The cation exchange method was slightly modified from that described in Fischer-Gödde et al. (2010, 2011). Instead of using a HCl-acetone mixture, 0.2 M HCl was employed here for the elution of Ru along with other HSE. After sample digestion, the *aqua regia* solution was carefully evaporated to near dryness at 80–100 °C on a hotplate, and was then taken to near dryness twice with 2 ml 9 M HCl and once with 1 ml 1 M HCl at slightly increased temperatures (100–130 °C). The samples were then dissolved in 5–10 ml 0.2 M HCl and loaded onto cation exchange columns filled with 10 ml of pre-cleaned BioRad AG50 W-X8 (100–200 mesh) resin, which has been equilibrated with 20 ml 0.2 M HCl. After loading, Ru together with Re, Ir, Pt, Rh and Pd were eluted in 14 ml 0.2 M HCl. The Ru yield from the cation exchange column is ~100%, but it is possible that a small fraction of the sample Ru was lost prior to column chemistry through volatilization from *aqua regia* during dry down of the digestion solution.

For samples digested by alkaline fusion and for the acid leachates and the insoluble residue of Allende, Ru was purified by distillation in a PFA distillation unit without prior cation exchange separation. The same distillation unit was also used for the purification of Ru from some iron meteorites, but this time after cation exchange chemistry.

2.2.1. Micro-distillation

The Ru cut from the cation column was dried down on a hotplate, re-dissolved in one drop of concentrated HCl and two drops of concentrated HNO_3, loaded into the lid of a conical 5 ml Savillex beaker and evaporated to dryness at 80 °C. Ruthenium was distilled as RuO_4 from a H_2SO_4-CrO_3 solution into a drop of HBr (Roy-Barman, 1993). The drop of HBr containing the Ru was evaporated to dryness, re-dissolved in a drop of concentrated nitric acid and diluted to 0.28 M HNO_3 for analysis. Initially some of the Ru cuts contained significant amounts of Cr after the micro-distillation, probably derived from splashes of the H_2SO_4-CrO_3 solution. Careful and slow heating of the sample largely suppressed the formation of such splashes. Tests with Cr-doped Ru standard solutions show that the Ru isotope measurements are not compromised by the presence of Cr, however, even if significant levels of Cr (Cr/Ru = 1) are present in the analyzed sample solution (E-Annex, Fig. EA1). Some samples also contained traces of Os after the micro distillation step, but the presence of Os would not affect the accuracy of the Ru isotope measurements up to Os/Ru ratios of ~2 (E-Annex, Fig. EA2).

Yield tests conducted with several Ru-doped reference samples (UB-N, BCR-2, BHVO-2, NIST 129c, NIST 361) show that the Ru yield for the entire procedure (sample digestion + cation exchange + micro-distillation) varies between ~40% and ~90%. The total procedural blank of the analytical protocol including sample digestion, column chemistry and micro-distillation is 69 ± 37 pg (1s.d., $n = 4$) and insignificant given the amount of Ru (>100 ng) present in each of the investigated meteorite samples.

2.2.2. PFA distillation unit

The distillation unit consists of 60 and 30 ml Savillex vials, sealed with 33 mm impinger closures, and connected with 1/8″ PFA tubing. A peristaltic pump was attached to the tube reaching into the 60 ml vial to generate a stream of air through the unit. The Ru is trapped in the 30 ml vial in a 3% H_2O_2 solution. In total four samples could be distilled in the unit at the same time. After the alkaline fusion, the digestion cake was soaked in Milli-Q H_2O and transferred to the 60 ml impinger PFA vials of the distillation unit. The solution was carefully neutralized by stepwise addition of 10–15 ml of a 1:1 H_2SO_4:H_2O solution. After the addition of 3.6 ml of an aqueous saturated CrO_3 solution, the sample was distilled on a hotplate for 6 h at 70–80 °C and RuO_4 was trapped in 10 ml of a 3% H_2O_2 solution. The distillation was continued for 6 h at 80 °C using a second beaker with 10 ml of 3% H_2O_2 trap solution. Ruthenium from both distillation steps was combined if significant amounts of Ru were still present in the second step. The H_2O_2 solution was evaporated to dryness and the sample dissolved in 0.28 M HNO_3 for analysis. The advantage of using H_2O_2 as the RuO_4 trap solution is that co-distilled OsO_4 from the sample is not reduced by H_2O_2 and hence passes through the trap as a gas (Westland and Beamish, 1954). The same distillation technique was used for some IIAB iron meteorites (Cinci, Holland Store, San Francisco), a sample of Grant (IIIAB), and one NIST 129c steel. Note that these samples have been passed through a cation exchange column prior to distillation.

The Ru yield from the distillation unit is 60–80% as tested with pure Ru standard solutions without prior fusion. For samples the yields might be slightly lower, because some Ru may have volatilized during sample digestion using the oxidizing alkaline fusion and because the sample matrix might have suppressed the oxidation and tetroxide formation in the reaction vial during distillation. The total procedural blank including sample decomposition by alkaline fusion and Ru purification by distillation is 41 ± 17 pg (1s.d., $n = 3$) and, hence, insignificant. One erratic high blank of ~2 ng Ru was observed, but even this blank is insignificant given that more than ~100 ng Ru were analyzed for each sample within the sample set of this blank.

2.3. Mass spectrometry

All Ru isotope measurements were performed using the ThermoScientific Neptune *Plus* MC-ICPMS in the Institut für Planetologie at the University of Münster. Samples were dissolved in 0.28 M HNO_3 and introduced into the mass spectrometer at an uptake rate of 60–70 µl/min using an ESI Microflow PFA nebulizer or a Glass Expansion MicroMist borosilicate nebulizer attached to a Cetac Aridus II desolvator. Initially an ESI Apex-Q was used as the sample introduction system, but was replaced by an Aridus II because of the lower oxide rates of the latter. The measurements were typically performed with a total ion beam intensity ranging from 7.5×10^{-11} to 4.4×10^{-10} A, which were obtained for ~100 ppb Ru using conventional Ni H-cones. For comparison some replicate measurements of NIST 129c and meteorite samples were also analyzed using an X-skimmer cone, which yields improved sensitivity with ion beam intensities ranging from 3.2×10^{-10} to 4.8×10^{-10} A for ~100 ppb Ru. Results obtained for both cone designs are generally consistent and no systematic bias was observed. However, using the X-skimmer cone much higher oxide rates were occasionally observed (10–15%, CeO/Ce) in comparison to the conventional H-cones (<<1%). All Ru isotope measurements were, therefore, conducted using conventional H-cones, given that sufficient amounts of Ru were available for precise isotope analysis. Only Ru from Allende leachates L1 and L6 was analyzed in a 20 ppb solution using an X-skimmer cone.

The Ru isotope measurements were performed in static mode and the seven stable Ru isotopes ^{96}Ru ^{99}Ru, ^{98}Ru, ^{101}Ru, ^{102}Ru, and ^{104}Ru as well as ^{97}Mo and ^{105}Pd were monitored simultaneously. All masses were measured in Faraday cups connected to amplifiers with 10^{11} Ω feedback resistors, except for the interference monitors ^{97}Mo and ^{105}Pd, for which amplifiers connected to 10^{12} Ω resistors were used. Each Ru isotope analysis consisted of an on-peak baseline measurement on a solution blank for 40 times 8.4 s followed by 100 integrations of 8.4 s each of the sample or standard solution. In case of the Allende leachates L2-L5 the measurements consisted of 40–100 integrations of 8.4 s on a 100 ppb solution and 50 integrations of 8.4 s on a 20 ppb solution for L1 and L6. Each sample analysis was bracketed by measurements of an in-house Ru solution standard (Alfa Aesar Ru), with samples and standards being analyzed at similar ion beam intensities that were matched to better than 20%. Mass bias was corrected by internal normalization to $^{99}Ru/^{101}Ru = 0.7450754$ (Chen et al., 2010) using the exponential law. This normalization was used because there are no significant isobaric interferences on both ^{99}Ru and ^{101}Ru and because nucleosynthetic isotope variations result in characteristic isotope patterns for this normalization (Chen et al., 2010). The Ru isotope data are reported as the part per 10,000 deviation from the mean value of the bracketing standard runs as follows:

$$\varepsilon^{i}\mathrm{Ru} = [(^{i}\mathrm{Ru}/^{101}\mathrm{Ru})_{\mathrm{sample}}/(^{i}\mathrm{Ru}/^{101}\mathrm{Ru})_{\mathrm{standard}} - 1] \times 10^{4}.$$

Isobaric interferences from Mo and Pd can occur on several Ru masses, and are most significant for ^{96}Ru (5.54%) and ^{98}Ru (1.87%) because of their lower abundances compared to ^{96}Mo (16.68%) and ^{98}Mo (24.13%). The accuracy and robustness of the interference corrections were tested by analyzing Ru standard solutions doped with various amounts of Mo and Pd (E-Annex, Fig. EA3). The tests demonstrate that the interference corrections are accurate for Mo/Ru ratios up to 5×10^{-4} and for Pd/Ru ratios up to 1×10^{-2}. For most of the analyzed meteorite samples much lower ratios were achieved, with Mo/Ru $< 2 \times 10^{-5}$ and Pd/Ru $< 1 \times 10^{-4}$, resulting in interference corrections that were always <4 ε-units for ^{98}Ru (and much smaller for all other isotope ratios). Because isobaric interferences from ^{96}Zr (2.80 %) on ^{96}Ru (5.54 %) could not be simultaneously monitored during the measurements, the amount of Zr present in the final Ru sample solutions was determined on a small aliquot using a quadruple ICPMS (ThermoScientific XSeries II), or in a pre-dilution on the MC-ICPMS before

the Ru isotope analysis. None of the analyzed samples had significant levels of Zr, limiting potential Zr interferences on mass 96 to less than 0.1 ε-units, *i.e.*, well within the analytical uncertainty of the ^{96}Ru measurements of ±0.45 ε^{96}Ru (see below).

3. RESULTS

3.1. Precision and accuracy of Ru isotope data

The accuracy and precision of the Ru isotope measurements were evaluated by replicate digestions and multiple analyses of different types of terrestrial reference materials, doped with ~500 to ~2000 ng Ru from the same Alfa Aesar solution standard used to bracket the Ru isotope measurements of samples. The terrestrial materials included the NIST 129c and 361 steels, peridotite UB-N and basalts BCR-2 and BHVO-2. The doped samples were processed through the whole purification procedure alongside each set of meteorites. All doped standards yielded ε^{i}Ru values of ~0, demonstrating that our analytical procedure leads to accurate Ru isotope results. The external reproducibility (2s.d.) of the Ru isotope analyses obtained for all processed reference samples (including 84 individual measurements from 18 digestions of 5 different reference samples) is ±0.45 ε^{96}Ru, ±0.52 ε^{98}Ru, ±0.13 ε^{100}Ru, ±0.15 ε^{102}Ru, and ±0.31 ε^{104}Ru (Table 1). This is an improvement by a factor of 2–5 compared to a previous Ru isotope study employing N-TIMS (Chen et al., 2010), for a similar amount of Ru consumed in a single analysis.

To further test our analytical method and to assess the Ru isotope composition of the Earth's mantle, we also analyzed a chromitite sample from the Shetland Ophiolite Complex in Scotland (O'Driscoll et al., 2012). The chromitites have high Ru concentrations of up to ~20 ppm, making it possible to determine the isotopic composition of mantle-derived Ru more directly compared to the analysis of Ru solution standards. Repeated analyses of the C3 chromitite (O'Driscoll et al., 2012) yielded ε^{i}Ru ~0, indicating that its Ru isotope composition is indistinguishable from that of the Alfa Aesar Ru solution standard. Moreover, the chromitite results provide further evidence that our analytical procedure produces accurate results.

3.2. Allende leachates

The Ru isotope data for leachates and an insoluble residue of Allende (Table 2) reveal large internal isotopic variations for ε^{96}Ru, ε^{98}Ru, ε^{100}Ru and ε^{102}Ru, well resolved from the terrestrial Ru standard (Fig. 1). Leach steps L3, L4 and L5 show Ru isotope patterns with negative anomalies in ε^{96}Ru and ε^{98}Ru and positive anomalies in ε^{100}Ru and ε^{102}Ru (Fig. 1). These patterns are similar to but of much smaller magnitude than those observed for presolar SiC grains, which are strongly enriched in *s*-process isotopes (Savina et al., 2004). The Ru isotope compositions of leachates L3, L4 and L5, therefore, most likely indicate excesses in *s*-process Ru nuclides relative to the terrestrial Ru standard. The Ru isotope pattern of leachate L2 is complimentary to those of leachates L3-5, and as such attributable to an *s*-deficit. Leachate L1 and the insoluble residue L6 exhibit less distinctive Ru isotope anomaly patterns with well-resolved anomalies observed only for ε^{100}Ru. In case of L6 this is surprising, because the insoluble residue should be strongly enriched in presolar phases and would, therefore, be expected to display large nucleosynthetic isotope anomalies.

3.3. Iron meteorites and chondrites

Consistent with a previous study (Chen et al., 2010), we find Ru isotope anomalies in most iron meteorites and chondrites (Table 3). The bulk meteorites are characterized by negative ε^{100}Ru and ε^{102}Ru values, and exhibit positive albeit not well-resolved ε^{96}Ru and ε^{98}Ru values (Fig. 1). Only the IAB iron meteorites and EL chondrites show no resolved Ru isotopic anomalies. The Ru isotope patterns of the bulk meteorites are similar to that of Allende leachate L2, suggesting that the bulk meteorites are characterized by a deficit in *s*-process Ru nuclides. However, we observe Ru isotope variations among samples from a given chemical group of magmatic iron meteorites, and these are unlikely to be nucleosynthetic in origin. This is because samples from a given group probably formed by fractional crystallization of a single, isotopically homogeneous metallic melt. It is noteworthy that the largest within-group deviations are observed for samples having long cosmic ray exposure (CRE) times. For instance, Ainsworth (IIAB), one of the most strongly irradiated iron meteorites (Voshage and Feldmann, 1979), displays elevated ε^{96}Ru, ε^{100}Ru, ε^{102}Ru and ε^{104}Ru values compared to the other investigated IIAB irons (Table 3). Likewise, the ε^{100}Ru of Carbo (IID), another strongly irradiated sample with ample evidence for strong irradiation effects, is higher than that of Rodeo, which is an only weakly irradiated IID iron (Table 3). These observations suggest that the within-group Ru isotope variations are caused by different CRE times. Note that the magnitude of cosmogenic effects in iron meteorites depends on several factors such as the duration of CRE and the location of a sample within the meteoroid. Consequently, neutron capture effects could vary for different samples of a given chemical group of iron meteorites, making it a likely process to generate the observed within-group Ru isotope variations.

The Ru isotopic data for the meteorites investigated in the present study show no evidence for radiogenic ^{98}Ru variations, which could potentially derive from the decay of short-lived ^{98}Tc. The lack of any resolvable radiogenic ^{98}Ru anomalies is consistent with results of previous studies and either reflects a low initial ^{98}Tc abundance of the solar system or is the result of limited Tc/Ru fractionations in bulk meteorites (Becker et al., 2002; Becker and Walker, 2003).

4. DISCUSSION

4.1. Meaning of the Ru isotopic anomalies

All the Ru isotope data are expressed as relative deviations from the isotopic composition measured for an Alfa

Table 1
Ruthenium isotope composition of Ru-doped reference samples.

Sample	N[a]	$\varepsilon^{96}Ru$[b]	$\varepsilon^{98}Ru$[b]	$\varepsilon^{100}Ru$[b]	$\varepsilon^{102}Ru$[b]	$\varepsilon^{104}Ru$[b]
NIST 129c #1	5	−0.05 ± 0.53	−0.02 ± 0.67	−0.02 ± 0.10	0.00 ± 0.22	0.02 ± 0.55
NIST 129c #2	7	−0.05 ± 0.31	0.19 ± 0.31	0.01 ± 0.10	0.03 ± 0.11	0.03 ± 0.36
NIST 129c #3	8	0.01 ± 0.29	0.14 ± 0.31	−0.02 ± 0.13	0.00 ± 0.10	0.02 ± 0.18
NIST 129c #4	9	0.05 ± 0.31	−0.12 ± 0.41	−0.06 ± 0.13	0.00 ± 0.12	0.02 ± 0.20
NIST 129c #5	7	−0.10 ± 0.37	0.03 ± 0.46	0.00 ± 0.13	0.04 ± 0.20	0.09 ± 0.32
NIST 129c #6	3	0.31 ± 0.45	0.19 ± 0.52	0.07 ± 0.13	0.07 ± 0.15	0.16 ± 0.31
NIST 129c #7	4	0.31 ± 0.28	−0.09 ± 0.40	−0.03 ± 0.12	0.01 ± 0.14	0.27 ± 0.17
NIST 129c #8[c]	2	0.45 ± 0.45	−0.07 ± 0.52	−0.07 ± 0.13	0.07 ± 0.15	0.46 ± 0.31
NIST 129c #9	4	0.07 ± 0.28	0.22 ± 0.60	−0.04 ± 0.13	0.06 ± 0.11	0.11 ± 0.32
NIST 361	5	−0.01 ± 0.31	0.03 ± 0.75	−0.06 ± 0.11	−0.04 ± 0.25	0.05 ± 0.38
UB-N #1	6	0.19 ± 0.32	0.02 ± 0.11	−0.03 ± 0.04	−0.01 ± 0.03	0.05 ± 0.07
UB-N #2	8	−0.12 ± 0.20	0.02 ± 0.24	−0.05 ± 0.03	−0.02 ± 0.03	0.02 ± 0.08
UB-N #3	4	0.07 ± 0.19	−0.21 ± 0.45	0.00 ± 0.03	0.03 ± 0.05	0.05 ± 0.07
UB-N #4[c,d]	3	0.44 ± 0.45	−0.13 ± 0.52	0.00 ± 0.13	0.00 ± 0.15	0.10 ± 0.31
UB-N #5[c,d]	1	0.23 ± 0.45	0.89 ± 0.52	−0.03 ± 0.13	−0.01 ± 0.15	0.24 ± 0.31
BCR-2 #1	3	0.26 ± 0.45	0.06 ± 0.52	0.01 ± 0.13	0.05 ± 0.15	0.18 ± 0.31
BCR-2 #2	4	0.07 ± 0.17	0.00 ± 0.19	0.09 ± 0.10	0.14 ± 0.07	0.16 ± 0.20
BHVO-2	5	0.01 ± 0.12	−0.10 ± 0.26	0.07 ± 0.03	0.09 ± 0.09	0.10 ± 0.22
	Mean all[*]	0.06	0.02	−0.01	0.02	0.08
	±2sd	0.45	0.52	0.13	0.15	0.31
	±95% conf.	0.05	0.06	0.01	0.02	0.03
	n	84	84	84	84	84

[a] Number of analyses of the same solution.
[b] Ruthenium isotope data are internally normalized to $^{99}Ru/^{101}Ru$ using the exponential law and are reported as deviation in parts per 10,000 from the terrestrial bracketing standard: $\varepsilon^{i}Ru = (^{i}Ru/^{101}Ru_{sample}/^{i}Ru/^{101}Ru_{standard} - 1) \times 10^{4}$. Uncertainties for samples measured more than triplicate are given as the 95% confidence interval. For samples measured once, twice and triplicate quoted errors represent the external uncertainty as defined by the standard deviation (2σ) deduced from repeated analysis of Ru doped reference samples (±2sd).
[c] Sample processed in Teflon distillation unit for Ru purification.
[d] Sample decomposed by alkaline fusion.
[*] Mean values calculated for pooled individual measurements ($n = 84$) from 18 digestions of 5 different reference samples (NIST 129c, NIST 361, UB-N, BCR-2, BHVO-2).

Table 2
Ruthenium isotope composition of acid leachates and an insoluble residue of Allende.

Leach step	N[a]	$\varepsilon^{96}Ru$[b]	$\varepsilon^{98}Ru$[b]	$\varepsilon^{100}Ru$[b]	$\varepsilon^{102}Ru$[b]	$\varepsilon^{104}Ru$[b]
L1	1	0.29 ± 0.47	5.55 ± 0.73	1.96 ± 0.16	0.51 ± 0.19	−0.03 ± 0.43
L2	2	2.12 ± 0.45	2.04 ± 0.52	−4.60 ± 0.13	−1.94 ± 0.15	0.17 ± 0.31
L3	1	−1.80 ± 0.45	−1.22 ± 0.52	3.83 ± 0.13	1.68 ± 0.15	0.01 ± 0.31
L4	1	−12.84 ± 0.45	−10.55 ± 0.52	30.21 ± 0.13	12.46 ± 0.15	−1.10 ± 0.31
L5	1	−4.40 ± 0.55	−3.65 ± 0.54	14.68 ± 0.20	5.97 ± 0.22	−0.86 ± 0.46
L6	1	0.90 ± 0.45	0.17 ± 0.52	1.84 ± 0.16	0.52 ± 0.17	0.39 ± 0.42

[a] Number of analyses of the same solution.
[b] Ruthenium isotope data are internally normalized to $^{99}Ru/^{101}Ru$ using the exponential law and are reported as deviation in parts per 10,000 from the terrestrial bracketing standard: $\varepsilon^{i}Ru = (^{i}Ru/^{101}Ru_{sample}/^{i}Ru/^{101}Ru_{standard} - 1) \times 10^{4}$. Quoted errors either reflect the external uncertainty as defined by the standard deviation (2σ) of repeated analysis of reference samples (Table 1) or the internal precision ($2\sigma_m$), whichever is larger.

Aesar Ru solution standard, and corrected for instrumental and natural mass-dependent isotope fractionation using the exponential law. However, not all mass-dependent isotope fractionations follow this law, meaning that for highly mass-fractionated samples the correction of natural isotope fractionations using the exponential law may result in an apparent mass-independent isotope anomaly (Young et al., 2002). For instance, small isotopic differences between solution standards and terrestrial samples for Ni (Steele et al., 2011) and Ti (Zhang et al., 2011) have been attributed to non-exponential isotope fractionations of the Ni and Ti in the solution standards. This does not seem to be the case for Ru, however, because any apparent mass-independent anomaly resulting from differences in mass fractionation behavior would have led to larger offsets in the measured $^{104}Ru/^{101}Ru$ compared to the $^{100}Ru/^{101}Ru$ ratios (both normalized to $^{99}Ru/^{101}Ru$), owing to the larger mass difference of the former ratio. The $\varepsilon^{104}Ru$ values of all meteorites analyzed in the present study are indistinguishable from the solution standard, however, in spite of well-resolved $\varepsilon^{100}Ru$ anomalies in the same samples (Fig. 1). Thus, there is no evidence in the Ru isotope data

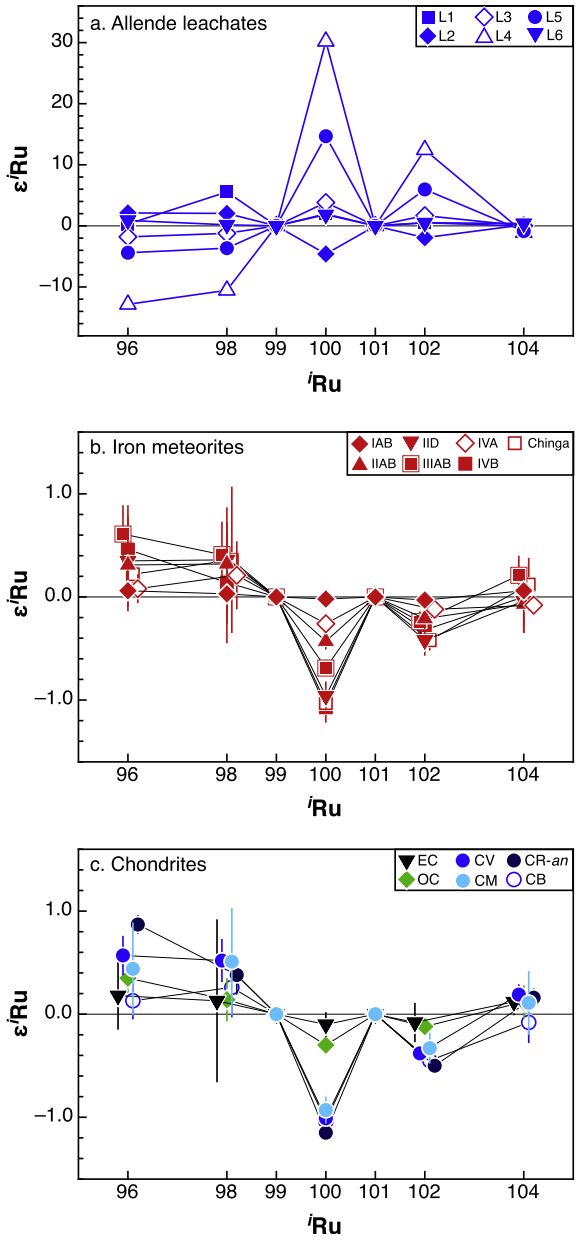

Fig. 1. Ruthenium isotope data for Allende leachates (a), iron meteorites (b), and chondrites (c) internally normalized to $^{99}Ru/^{101}Ru$ to correct for instrumentally induced mass bias. $\varepsilon^{i}Ru$ values correspond to the deviation in parts per 10.000 of a measured $^{i}Ru/^{101}Ru$ ratio from the terrestrial $^{i}Ru/^{101}Ru$ (see Table 1 footer). Data shown for iron meteorites and chondrites represent group averages given in Table 4. Data for IIAB, IID, IIIAB, and IVB irons shown in (b) have been corrected for neutron capture effects (as discussed in text, Section 4.4.). Only Allende and Murchison data obtained by alkaline fusion are shown in (c) for reasons discussed in text (Section 4.3.).

for significant mass-independent anomalies resulting from different mass fractionation behavior. Moreover, in $\varepsilon^{i}Ru$–$\varepsilon^{100}Ru$ diagrams the meteorite data define linear correlation lines passing through zero, i.e., through the composition of the Alfa Aesar solution standard (see below, Sections 4.2 and 4.5). This would not be the case if the Ru isotope composition of the solution standard would show significant mass-independent isotope anomalies relative to the BSE composition, because then the solution standard should plot off the $\varepsilon^{i}Ru$–$\varepsilon^{100}Ru$ correlation line defined by the meteorites. In addition, the only terrestrial sample analyzed as part of the present study—a chromitite from the Shetland Ophiolite Complex in Scotland (O'Driscoll et al., 2012)—yielded $\varepsilon^{i}Ru \sim 0$, indicating that the Ru isotope composition of the solution standard is indistinguishable from that of the Earth's mantle (Table 3).

Fujii et al. (2006) argued that at least some of the Ru isotope anomalies in meteorites are caused by the nuclear field shift effect. These authors showed that the Ru isotope anomalies obtained for Murchison (CM2) by Chen et al. (2010) are consistent with those expected from the nuclear field shift effect, in particular with the observation that the measured $\varepsilon^{104}Ru$ anomaly is about two times larger than its $\varepsilon^{100}Ru$ anomaly. Because the nuclear field shift effect would lead to Ru isotope anomalies decreasing in the order $\varepsilon^{104}Ru > \varepsilon^{102}Ru > \varepsilon^{100}Ru$ (Fujii et al., 2006), we can use our data to assess the significance of this effect in generating the Ru isotope anomalies observed in the investigated meteorite sample suite. In fact, the Ru isotope anomalies of the meteorites investigated in the present study decrease in the order $\varepsilon^{100}Ru > \varepsilon^{102}Ru > \varepsilon^{104}Ru$, exactly opposite to the order of anomalies expected from the nuclear field shift effect. In contrast, this order of anomalies is consistent with the expected isotope variations for a heterogeneous distribution of *s*- and *r*-process Ru nuclides (Fig. 1). Moreover, in $\varepsilon^{i}Ru$ *vs.* $\varepsilon^{100}Ru$ plots (Figs. 2 and 3), the meteorite data define linear correlations, which most likely represent mixing lines between an *s*-enriched (positive $\varepsilon^{100}Ru$ and $\varepsilon^{102}Ru$ and negative $\varepsilon^{96}Ru$ and $\varepsilon^{98}Ru$) and a complementary *s*-depleted component. Thus, the most straightforward interpretation is that the Ru isotope variations are nucleosynthetic in origin and reflect variable contributions of at least two distinct nucleosynthetic components.

4.2. Carrier of *s*-process Ru in Allende and comparison to *s*-process model calculations

The directions and slopes of the $\varepsilon^{i}Ru$ *vs.* $\varepsilon^{100}Ru$ correlation lines defined by the leachate and bulk meteorite data provide insights in the nature of presolar component(s) present in the early solar system and may ultimately allow identifying a specific component that causes the observed isotopic variability. Dauphas et al. (2004) derived equations for mixing lines for internally normalized isotope ratios in epsilon-epsilon space. For Ru this takes the form:

$$\varepsilon^{i}Ru = \frac{\rho^{i}Ru - \rho^{99}Ru \cdot \mu^{i}Ru}{\rho^{100}Ru - \rho^{99}Ru \cdot \mu^{100}Ru} \cdot \varepsilon^{100}Ru \quad (1)$$

where the parameter $\rho^{i}Ru$ represents the *s*-process composition relative to the terrestrial Ru isotope composition:

$$\rho^{i}Ru = \frac{(^{i}Ru/^{101}Ru)_{s}}{(^{i}Ru/^{101}Ru)_{\oplus}} - 1 \quad (2)$$

Table 3
Ruthenium isotope composition of a terrestrial chromitite and bulk meteorites.

Group	Sample	Method[a]	N[b]	$\varepsilon^{96}Ru$[c]	$\varepsilon^{98}Ru$[c]	$\varepsilon^{100}Ru$[c]	$\varepsilon^{102}Ru$[c]	$\varepsilon^{104}Ru$[c]	$\varepsilon^{196}Pt$[d]
Terrestrial									
Chromitite[f]	C3	AF; 3	3	−0.08 ± 0.45	−0.05 ± 0.52	0.02 ± 0.13	−0.09 ± 0.15	−0.34 ± 0.31	
	Duplicate	Acid; 1	5	−0.01 ± 0.20	0.05 ± 0.25	0.05 ± 0.10	0.07 ± 0.10	0.12 ± 0.18	
	Mean[e]			−0.04 ± 0.11	0.01 ± 0.19	0.04 ± 0.06	0.01 ± 0.09	−0.05 ± 0.22	
Iron meteorites									
IAB	Canyon Diablo	Acid; 1	1	0.26 ± 0.45	0.03 ± 0.52	−0.08 ± 0.13	−0.11 ± 0.15	−0.05 ± 0.31	
	Duplicate	Acid; 1	1	−0.04 ± 0.45	0.08 ± 0.52	−0.02 ± 0.13	0.00 ± 0.15	0.11 ± 0.31	
	Odessa	Acid; 1	2	0.18 ± 0.45	0.30 ± 0.52	−0.08 ± 0.13	−0.01 ± 0.15	0.06 ± 0.31	
	Campo del Cielo	Acid; 1	1	0.19 ± 0.45	0.44 ± 0.52	−0.06 ± 0.13	−0.10 ± 0.15	−0.06 ± 0.31	
	Duplicate	Acid; 1	3	−0.10 ± 0.45	−0.29 ± 0.52	0.04 ± 0.13	−0.01 ± 0.15	0.13 ± 0.31	
IAB mean[e]				0.06 ± 0.20	0.03 ± 0.29	−0.02 ± 0.06	−0.03 ± 0.04	0.06 ± 0.09	
IIAB	North Chile	Acid; 1	1	0.51 ± 0.45	0.42 ± 0.52	−0.47 ± 0.13	−0.06 ± 0.15	0.39 ± 0.31	
	Duplicate	Acid; 1	5	0.23 ± 0.32	0.29 ± 0.25	−0.44 ± 0.04	−0.16 ± 0.04	−0.01 ± 0.14	
	Holland Store	Acid; 2	5	0.56 ± 0.34	0.45 ± 0.79	−0.40 ± 0.08	−0.18 ± 0.05	0.05 ± 0.09	
	Cinci	Acid; 2	4	0.42 ± 0.15	0.43 ± 0.34	−0.49 ± 0.14	−0.21 ± 0.18	0.33 ± 0.19	
	San Francisco	Acid; 2	1	0.11 ± 0.45	−0.12 ± 0.52	−0.59 ± 0.13	−0.14 ± 0.15	0.33 ± 0.31	
	Coahuila	Acid; 1	4	0.44 ± 0.29	0.29 ± 0.25	−0.43 ± 0.17	−0.18 ± 0.21	0.28 ± 0.38	
	Duplicate	Acid; 1	6	0.17 ± 0.11	0.25 ± 0.34	−0.46 ± 0.05	−0.20 ± 0.08	−0.07 ± 0.09	
	Braunau	Acid; 1	6	0.44 ± 0.25	0.15 ± 0.59	−0.47 ± 0.06	−0.15 ± 0.02	0.22 ± 0.07	
	Duplicate	Acid; 1	7	0.27 ± 0.20	0.50 ± 0.26	−0.40 ± 0.07	−0.24 ± 0.05	−0.18 ± 0.12	
	Duplicate	Acid; 1	1	0.35 ± 0.45	−0.02 ± 0.52	−0.42 ± 0.13	−0.20 ± 0.15	−0.09 ± 0.31	
	Mean[e]			0.35 ± 0.13	0.31 ± 0.25	−0.43 ± 0.04	−0.20 ± 0.03	0.00 ± 0.13	0.03 ± 0.05
	Edmonton	Acid; 1	7	0.32 ± 0.25	0.30 ± 0.35	−0.41 ± 0.04	−0.14 ± 0.05	0.09 ± 0.12	
	Duplicate	Acid; 1	4	0.34 ± 0.32	0.24 ± 0.36	−0.41 ± 0.16	−0.17 ± 0.08	0.12 ± 0.10	
	Mean[e]			0.33 ± 0.16	0.28 ± 0.22	−0.41 ± 0.04	−0.15 ± 0.03	0.10 ± 0.07	0.01 ± 0.03
	Sikhote Alin	Acid; 1	4	0.50 ± 0.18	0.54 ± 0.19	−0.30 ± 0.06	−0.13 ± 0.10	−0.01 ± 0.11	
	Duplicate	Acid; 1	3	0.60 ± 0.45	0.58 ± 0.52	−0.28 ± 0.13	−0.12 ± 0.15	−0.01 ± 0.31	
	Mean[e]			0.54 ± 0.16	0.56 ± 0.17	−0.29 ± 0.05	−0.12 ± 0.05	−0.01 ± 0.08	0.27 ± 0.07
	Ainsworth	Acid; 1	3	1.34 ± 0.45	0.86 ± 0.52	0.14 ± 0.13	0.35 ± 0.15	1.24 ± 0.31	1.04 ± 0.07
IID	Rodeo	Acid; 1	5	0.35 ± 0.42	0.36 ± 0.17	−0.96 ± 0.07	−0.42 ± 0.11	−0.04 ± 0.30	0.00 ± 0.11
	Carbo	Acid; 1	7	0.65 ± 0.13	0.55 ± 0.33	−0.66 ± 0.05	−0.19 ± 0.07	0.23 ± 0.13	
	Duplicate	Acid; 1	5	0.43 ± 0.30	0.43 ± 0.70	−0.60 ± 0.09	−0.20 ± 0.14	0.09 ± 0.18	
	Mean[e]			0.56 ± 0.14	0.50 ± 0.28	−0.63 ± 0.04	−0.19 ± 0.06	0.17 ± 0.10	0.74 ± 0.07
IIIAB	Cape York (Agpalilik)	Acid; 1	5	0.40 ± 0.16	0.30 ± 0.37	−0.70 ± 0.10	−0.22 ± 0.07	0.25 ± 0.17	
	Duplicate	Acid; 1	1	0.34 ± 0.45	0.32 ± 0.52	−0.74 ± 0.13	−0.25 ± 0.15	0.13 ± 0.31	
	Mean[e]			0.39 ± 0.12	0.30 ± 0.28	−0.71 ± 0.08	−0.23 ± 0.05	0.23 ± 0.14	0.01 ± 0.07
	Grant A	Acid; 2	2	0.77 ± 0.45	0.71 ± 0.52	−0.57 ± 0.13	−0.21 ± 0.15	0.16 ± 0.31	0.13 ± 0.07
	Grant B	Acid; 1	1	0.61 ± 0.45	0.34 ± 0.52	−0.69 ± 0.13	−0.26 ± 0.15	0.16 ± 0.31	0.06 ± 0.07
	Henbury	Acid; 1	5	0.90 ± 0.15	0.53 ± 0.42	−0.62 ± 0.04	−0.17 ± 0.05	0.39 ± 0.06	0.15 ± 0.07
	Charcas	Acid; 1	4	0.66 ± 0.53	0.70 ± 0.28	−0.44 ± 0.10	−0.07 ± 0.07	0.36 ± 0.14	0.43 ± 0.03
	Boxhole	Acid; 1	4	0.72 ± 0.38	0.53 ± 0.31	−0.57 ± 0.05	−0.19 ± 0.11	0.26 ± 0.15	0.45 ± 0.07

IVA	Gibeon	Acid; 1	2	0.04 ± 0.45	0.03 ± 0.52	−0.27 ± 0.13	−0.11 ± 0.15	−0.10 ± 0.31	
	Duplicate	Acid; 1	2	0.13 ± 0.45	0.01 ± 0.52	−0.29 ± 0.13	−0.04 ± 0.15	−0.02 ± 0.31	
	Muonionalusta	Acid; 1	2	0.00 ± 0.45	0.35 ± 0.52	−0.21 ± 0.13	−0.18 ± 0.15	−0.18 ± 0.31	
	Duplicate	Acid; 1	2	0.14 ± 0.45	0.43 ± 0.52	−0.27 ± 0.13	−0.13 ± 0.15	−0.02 ± 0.31	
IVA mean[e]				0.08 ± 0.14	0.21 ± 0.33	−0.26 ± 0.04	−0.12 ± 0.05	−0.08 ± 0.10	
IVB	Santa Clara	Acid; 1	4	0.12 ± 0.38	0.43 ± 0.41	−0.87 ± 0.07	−0.31 ± 0.04	0.09 ± 0.19	
	Duplicate	Acid; 1	4	0.39 ± 0.49	0.29 ± 0.53	−0.86 ± 0.08	−0.27 ± 0.10	0.22 ± 0.21	
	Duplicate	Acid; 1	3	0.77 ± 0.45	0.53 ± 0.52	−0.92 ± 0.13	−0.31 ± 0.15	0.36 ± 0.31	
	Mean[e]			0.39 ± 0.23	0.41 ± 0.19	−0.88 ± 0.03	−0.30 ± 0.03	0.21 ± 0.10	0.43 ± 0.07
	Tavallah Valley	Acid; 1	3	0.33 ± 0.45	0.31 ± 0.52	−0.91 ± 0.13	−0.38 ± 0.15	0.05 ± 0.31	
	Duplicate	Acid; 1	4	0.41 ± 0.34	0.33 ± 0.32	−0.97 ± 0.06	−0.24 ± 0.16	0.46 ± 0.29	
	Mean[e]			0.38 ± 0.15	0.32 ± 0.15	−0.94 ± 0.05	−0.30 ± 0.10	0.29 ± 0.24	0.26 ± 0.07
	Cape of Good Hope	Acid; 1	3	0.06 ± 0.45	0.23 ± 0.52	−0.85 ± 0.13	−0.35 ± 0.15	−0.12 ± 0.31	
	Duplicate	Acid; 1	4	0.13 ± 0.17	0.22 ± 0.15	−0.85 ± 0.14	−0.33 ± 0.15	−0.08 ± 0.28	
	Dumont	Acid; 1	4	0.85 ± 0.14	0.16 ± 0.50	−0.90 ± 0.09	−0.31 ± 0.10	0.28 ± 0.17	0.38 ± 0.07
	Iquique	Acid; 1	5	0.54 ± 0.07	0.31 ± 0.12	−0.87 ± 0.06	−0.37 ± 0.08	0.06 ± 0.18	0.42 ± 0.07
	Tinnie	Acid; 1	5	0.83 ± 0.18	0.53 ± 0.41	−0.94 ± 0.03	−0.32 ± 0.08	0.40 ± 0.18	
	Tlacotepec	Acid; 1	6	0.36 ± 0.10	0.51 ± 0.20	−0.67 ± 0.06	−0.30 ± 0.06	−0.13 ± 0.13	0.84 ± 0.07
Ungrouped	Chinga	Acid; 1	1	0.25 ± 0.45	−0.61 ± 0.52	−1.08 ± 0.13	−0.46 ± 0.15	0.24 ± 0.31	
	Duplicate	Acid; 1	1	0.35 ± 0.45	0.51 ± 0.52	−1.01 ± 0.13	−0.52 ± 0.15	−0.23 ± 0.31	
	Duplicate	Acid; 1	3	0.26 ± 0.45	0.78 ± 0.52	−1.03 ± 0.13	−0.38 ± 0.15	0.13 ± 0.31	
	Mean[e]			0.22 ± 0.18	0.36 ± 0.71	−1.03 ± 0.04	−0.42 ± 0.10	0.12 ± 0.26	
Ordinary chondrites									
H4	Ochansk	CT; 1	1	0.66 ± 0.45	0.41 ± 0.52	−0.30 ± 0.13	−0.22 ± 0.15	−0.20 ± 0.31	
H4	Bath	CT; 1	2	0.54 ± 0.45	−0.03 ± 0.52	−0.32 ± 0.13	−0.05 ± 0.15	0.43 ± 0.31	
	Duplicate	CT; 1	1	0.33 ± 0.45	−0.38 ± 0.52	−0.34 ± 0.13	−0.11 ± 0.15	0.06 ± 0.31	
H4	Monroe	CT; 1	1	0.40 ± 0.45	0.18 ± 0.52	−0.27 ± 0.13	−0.09 ± 0.15	0.26 ± 0.31	
	Duplicate	CT; 1	2	0.11 ± 0.45	0.16 ± 0.52	−0.25 ± 0.13	−0.12 ± 0.15	0.15 ± 0.31	
H4	Forest Vale	CT; 1	1	0.25 ± 0.45	0.42 ± 0.52	−0.26 ± 0.13	−0.11 ± 0.15	0.06 ± 0.31	
H5	Pantar	CT; 1	2	0.28 ± 0.45	0.24 ± 0.52	−0.32 ± 0.13	−0.15 ± 0.15	−0.05 ± 0.31	
Ordinary chondrite mean[e]				0.35 ± 0.14	0.14 ± 0.21	−0.30 ± 0.03	−0.12 ± 0.04	0.12 ± 0.16	
Enstatite chondrites									
EL6	Daniel's Kuil	CT; 1	1	0.21 ± 0.45	0.47 ± 0.52	−0.16 ± 0.13	−0.21 ± 0.15	−0.01 ± 0.31	
EL6	Khairpur	CT; 1	2	0.15 ± 0.45	0.32 ± 0.52	−0.04 ± 0.13	0.01 ± 0.15	0.18 ± 0.31	
	Duplicate	CT; 1	1	0.23 ± 0.45	−0.59 ± 0.52	−0.14 ± 0.13	−0.11 ± 0.15	0.12 ± 0.31	
EL chondrite mean[e]				0.18 ± 0.33	0.13 ± 0.79	−0.10 ± 0.12	−0.08 ± 0.19	0.12 ± 0.13	
Carbonaceous chondrites									
CV3	Allende A[*]	CT; 1	1	0.81 ± 0.45	0.57 ± 0.52	−2.06 ± 0.13	−0.78 ± 0.15	0.11 ± 0.31	
	Duplicate	CT; 1	2	0.78 ± 0.45	0.24 ± 0.52	−1.44 ± 0.13	−0.59 ± 0.15	0.05 ± 0.31	
	Duplicate	AF; 3	1	0.88 ± 0.45	0.62 ± 0.52	−1.07 ± 0.13	−0.49 ± 0.15	0.23 ± 0.31	
	Allende (MS-A)[#]	CT; 1	2	0.38 ± 0.45	−0.16 ± 0.52	−1.32 ± 0.13	−0.55 ± 0.15	0.11 ± 0.31	
	Duplicate	CT; 1	2	0.34 ± 0.45	0.57 ± 0.52	−1.41 ± 0.13	−0.62 ± 0.15	0.00 ± 0.31	
	Duplicate	AF; 3	2	0.88 ± 0.45	0.46 ± 0.52	−1.04 ± 0.13	−0.33 ± 0.15	0.17 ± 0.31	
	Duplicate	AF; 3	2	0.29 ± 0.45	0.58 ± 0.52	−1.01 ± 0.13	−0.44 ± 0.15	0.04 ± 0.31	

(*continued on next page*)

Table 3 (*continued*)

Group	Sample	Method[a]	N[b]	ε^{96}Ru[c]	ε^{98}Ru[c]	ε^{100}Ru[c]	ε^{102}Ru[c]	ε^{104}Ru[c]	ε^{196}Pt[d]
	Duplicate	AF; 3	3	0.56 ± 0.45	0.71 ± 0.52	−1.00 ± 0.13	−0.40 ± 0.15	0.15 ± 0.31	
	Duplicate	AF; 3	2	0.43 ± 0.45	0.21 ± 0.52	−0.96 ± 0.13	−0.29 ± 0.15	0.39 ± 0.31	
CV3 mean[e]	(AF data only)			0.57 ± 0.19	0.52 ± 0.21	−1.01 ± 0.05	−0.38 ± 0.05	0.19 ± 0.10	
CM	Murchison (CB)	CT; 1	2	1.14 ± 0.45	0.66 ± 0.52	−3.37 ± 0.13	−1.25 ± 0.15	0.38 ± 0.31	
	Murchison (MS)	AF; 3	3	0.44 ± 0.45	0.51 ± 0.52	−0.93 ± 0.13	−0.33 ± 0.15	0.11 ± 0.31	
CB	Gujba metal	Acid; 1	3	0.11 ± 0.45	0.24 ± 0.52	−1.03 ± 0.13	−0.41 ± 0.15	0.01 ± 0.31	
	Duplicate	Acid; 1	3	0.14 ± 0.45	0.29 ± 0.52	−1.06 ± 0.13	−0.50 ± 0.15	−0.18 ± 0.31	
	Mean[e]			0.13 ± 0.18	0.26 ± 0.29	−1.04 ± 0.04	−0.45 ± 0.10	−0.08 ± 0.20	
CR-an	Tafassasset metal	Acid; 1	5	0.87 ± 0.09	0.38 ± 0.19	−1.15 ± 0.04	−0.50 ± 0.03	0.16 ± 0.09	

[a] Method column indicates technique used for digestion (Acid: table top digestion on hotplate; CT: Carius tube; AF: alkaline fusion) and Ru purification (1: ion exchange + micro distillation; 2: ion exchange + Teflon distillation unit; 3: Teflon distillation unit without prior ion exchange).

[b] Number of analyses of the same solution.

[c] Ruthenium isotope data are internally normalized to $^{99}Ru/^{101}Ru$ using the exponential law and are reported as deviation in parts per 10,000 from the terrestrial bracketing standard: $\varepsilon^{i}Ru = ({}^{i}Ru/{}^{101}Ru_{sample}/{}^{i}Ru/{}^{101}Ru_{standard} - 1) \times 10^{4}$. Uncertainties for samples measured more than triplicate are given as the 95% confidence interval. For samples measured once, twice and triplicate quoted errors reflect the external uncertainty as defined by the standard deviation (2s.d.) of repeated analysis of reference samples (Table 1).

[d] The ε^{196}Pt data from Kruijer et al. (2013a, 2014) and Matthes et al. (2014, 2015) were determined for samples from the same digestion solution or samples cut in close contact to the those used for Ru isotope analysis.

[e] Mean values calculated for pooled individual measurements from replicate digestions. Uncertainties are calculated at the 95% confidence interval.

[f] Chromitite powder (C3) from O'Driscoll et al. (2012).

[*] Allende powder used also for Mo isotope analysis in Burkhardt et al. (2011).

[#] Allende powder prepared at the Institute for Planetology in Münster from a ~100 g sample of Allende.

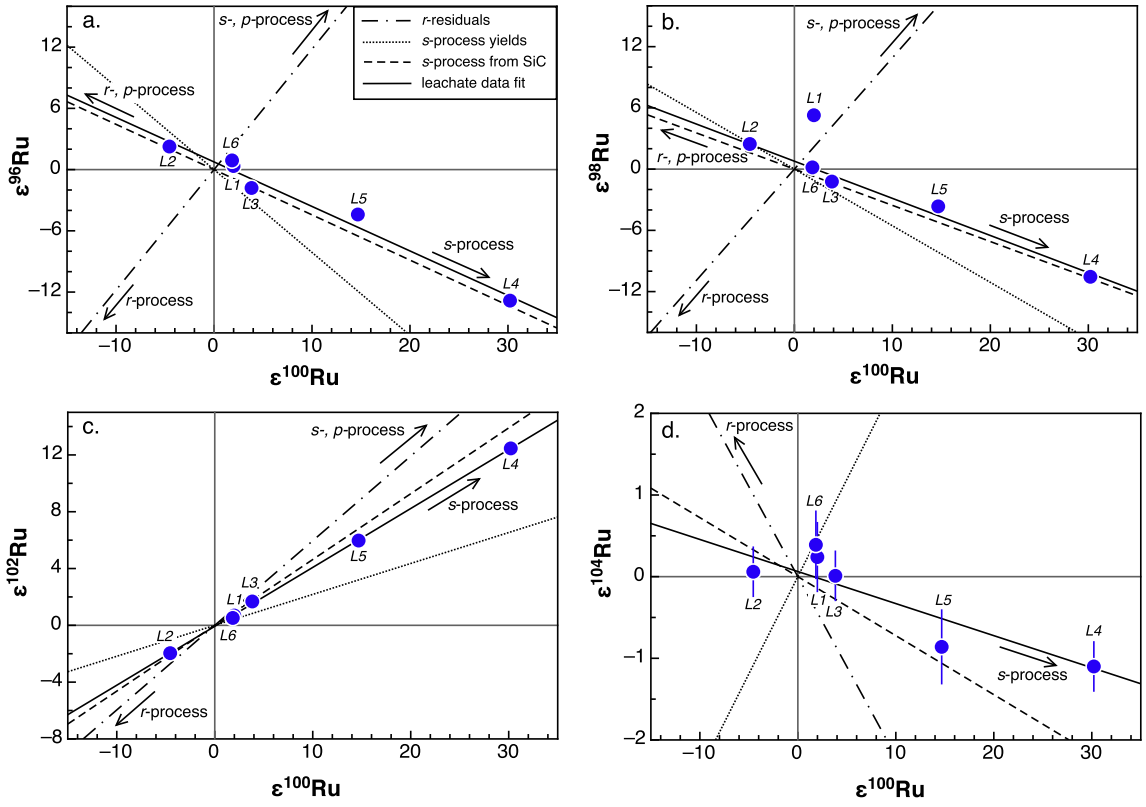

Fig. 2. ε^{i}Ru *vs.* ε^{100}Ru for Allende leachates (L1-L5) and the insoluble residue (L6) in comparison to mixing lines between presumed *s*-, *r*- and *p*-process components and the terrestrial Ru isotope composition. Broken lines represent mixing lines between terrestrial Ru and an *s*-process component as defined by Ru isotope data for SiC (dashed line, Savina et al., 2004); calculated *s*-process yields (dotted line, Bisterzo et al., 2011) and corresponding *r*-process residuals (dashed-dotted line). Solid lines represent linear regressions of ε^{96}Ru (a), ε^{98}Ru (b), ε^{102}Ru (c) and ε^{104}Ru (d) *vs.* ε^{100}Ru calculated using ISOPLOT (Ludwig, 2003) yielding slopes of -0.44 ± 0.09, -0.39 ± 0.18, 0.415 ± 0.006, and -0.04 ± 0.01, respectively (Table 5).

and μ^{i}Ru is the mass difference of the isotope ratio relative to that of the normalizing pair used for correction of instrumental mass fractionation:

$$\mu^{i}\mathrm{Ru} = \frac{i - 101}{99 - 101} \tag{3}$$

Information about the *s*-process Ru isotope composition is provided by data for mainstream circumstellar SiC grains (Savina et al., 2004), for which the calculated ρ^{i}Ru values are 0.40, 4.71, 1.89 and –0.926 for $i = 99$, 100, 102 and 104, respectively. No ^{96}Ru and ^{98}Ru data are reported in Savina et al. (2004), but the ρ^{i}Ru values for these two isotopes can be assumed to be −1 because ^{96}Ru and ^{98}Ru are not produced in the *s*-process. Additional constraints come from *s*-process production models (e.g., Arlandini et al., 1999; Bisterzo et al., 2011), for which the calculated ρ^{i}Ru values are 1.52, 6.67, 0.53 and −0.87 for $i = 99$, 100, 102 and 104, respectively (Bisterzo et al., 2011).

In ε^{i}Ru-ε^{100}Ru plots (Fig. 2) the Allende leachates (except L1) plot on single mixing lines between *s*-process–enriched and –depleted components, indicating that the distinct isotope compositions tapped in each leach step largely reflect the variable distribution of a single *s*-process component. They could alternatively reflect uneven mixing of a presolar component containing *p*- and *r*-process Ru nuclides in solar proportions. It is very unlikely, however, that such a (presolar) component exists, because there is no reason that a nucleosynthetic process should produce *p*- and *r*-process isotopes in exactly solar proportions (Dauphas et al., 2002a). Also shown in Fig. 2 are mixing lines between terrestrial Ru and presumed *s*-process components having a composition as inferred from either *s*-process production models or from measurements of presolar SiC (Savina et al., 2004). The Allende leachates (except L1) plot on mixing lines between terrestrial Ru and SiC and are, therefore, best explained by the varying release of *s*-process Ru from SiC grains or another presolar phase with a similar *s*-process composition (Fig. 2). In contrast, mixing with a presolar component having a composition as inferred from *s*-process production models does not provide a good fit to the Allende leachate data. Thus, either the true *s*-process composition is somewhat different from the modeled one, or the *s*-process composition of the products synthesized during different stages of stellar evolution changed.

The largest *s*-excess (i.e., the highest ε^{100}Ru) is already released by treatment with HF-HCl (leach step L4) (Fig. 2), although SiC is highly insoluble and, therefore, not expected to be dissolved in this leach step. Moreover, the insoluble residue remaining after the sequential leaching

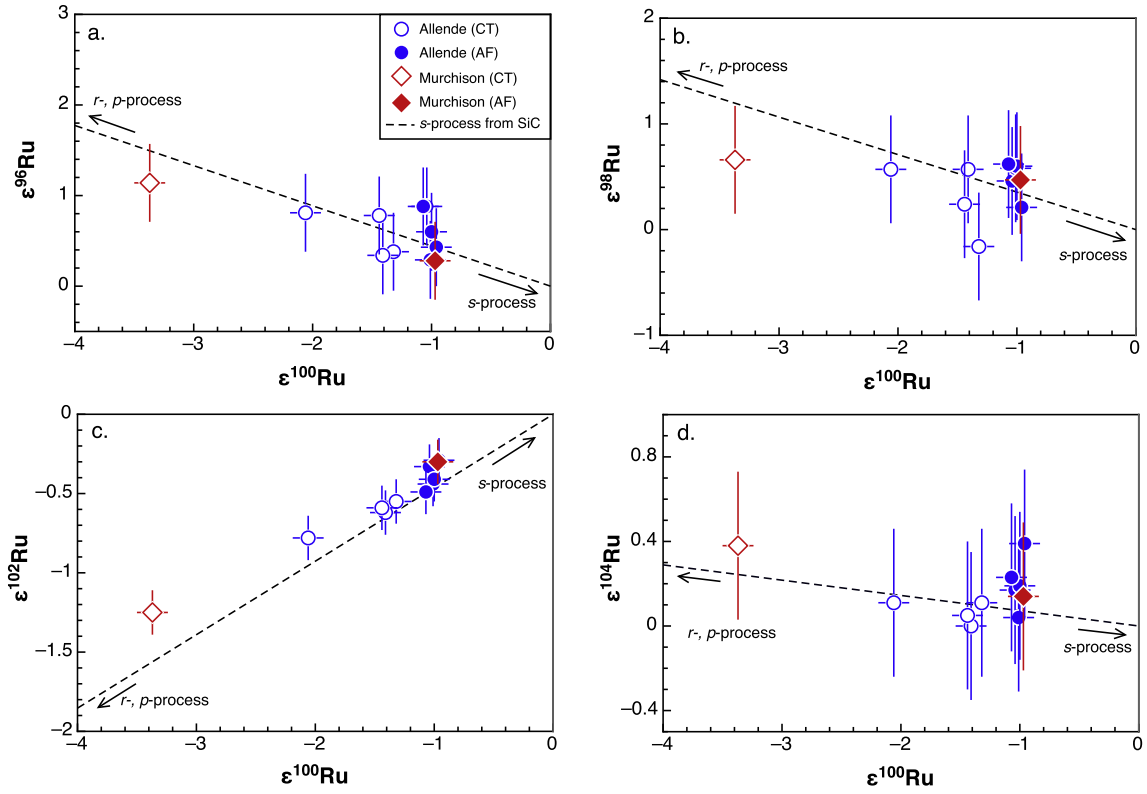

Fig. 3. Ruthenium isotope data shown in ε^{i}Ru *vs.* ε^{100}Ru spaces for replicate analyses of Allende and Murchison sample powders using different dissolution methods (CT = Carius tube digestion, AF = alkaline fusion). Dashed lines represent mixing lines between an *s*-process component as defined by Ru isotope data for SiC from Savina et al. (2004) and terrestrial Ru. Ruthenium isotope data from Carius tube digestions (open symbols) display considerably more scatter in ε^{i}Ru *vs.* ε^{100}Ru spaces than data obtained on fused sample powders (filled symbols).

(sample L6) exhibits only a very small *s*-excess, although SiC grains are typically enriched in the insoluble residue of primitive chondrites (Amari et al., 1995). This may suggest that the *s*-process Ru in Allende is hosted in more soluble presolar phases (e.g., silicates). Alternatively, *s*-process Ru may have been released from SiC grains and redistributed by nebular or parent body processes, consistent with the low abundance of SiC grains in Allende compared to more primitive chondrites (e.g., Huss and Lewis, 1995).

Sample L1 and to a lesser extent also L6 plot slightly off the ε^{i}Ru-ε^{100}Ru correlation lines defined by the other Allende leachates, indicating the presence of a third nucleosynthetic component in Allende. Both samples show evidence for an *s*-excess (i.e., positive ε^{100}Ru), but lack the expected negative ε^{96}Ru and ε^{98}Ru. This may indicate an excess in *p*-process Ru in addition to the *s*-excess or, alternatively a coupled *r*-deficit and *p*-excess. Clearly, more work is needed to unravel the nature of this component.

4.3. Ru isotopic composition of bulk chondrites

For bulk samples of Allende and Murchison, we observe larger and more variable Ru isotopic anomalies in samples decomposed using Carius tubes (*CT*) in comparison to those processed by alkaline fusion (*AF*). For both chondrites, the samples decomposed by *CT* display a deficit in *s*-process Ru compared to those processed by *AF*, indicating that an *s*-process carrier remained undissolved by the *CT* digestion, while it has been dissolved in the samples processed by *AF* (Fig. 3). During the sequential dissolution of Allende the largest *s*-excess occurs in leachates L4 and L5, the two leachates employing HF. A significant fraction of the *s*-process Ru in Allende, therefore, is hosted in HF-soluble components (see above). These components most likely were resistant to the *aqua regia* digestion by *CT*, which did not use any HF. Exclusion of some of the *s*-process-rich Ru tapped by leachates L4 and L5 then leads to the larger *s*-deficit observed for the samples dissolved by *CT* compared to those processed by *AF*. Our results for Ru are consistent with previous studies showing that primitive chondrites decomposed using *aqua regia* inside *CT* display a deficit in *s*-process Os isotopes compared to the same samples processed by *AF* (Brandon et al., 2005; Yokoyama et al., 2007; van Acken et al., 2011). Taken together, these results stress the importance of employing a complete digestion method when determining the isotope composition of bulk primitive chondrites. Note that all other chondrites investigated in the present study either are thermally metamorphosed (ordinary and enstatite chondrites, Tafassasset) or formed by condensation from a

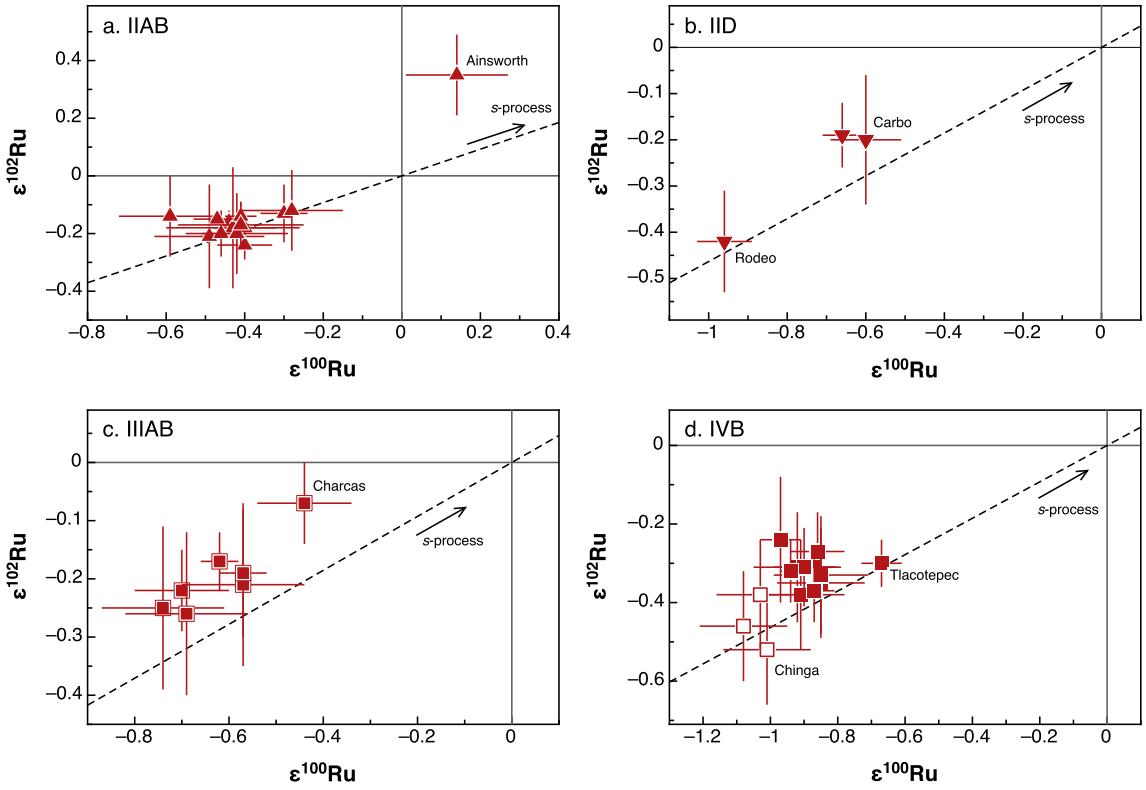

Fig. 4. Ruthenium isotope data for the IIAB (a.), IID (b.), IIIAB (c.) and IVB (d.) iron meteorites shown in ε^{102}Ru *vs.* ε^{100}Ru space. The predicted effect from the neutron capture model on ε^{100}Ru and ε^{102}Ru shifts the samples along the *s*-process mixing line (dashed line) as defined from Ru isotope data for SiC grains (Savina et al., 2004).

metal vapor plume (CB chondrite Gujba). In these samples no presolar phases are present, and so the *CT* digestion is sufficient to release the entire sample Ru.

The Ru isotope anomalies in chondrites decrease in the order carbonaceous > ordinary > enstatite chondrites. Note that for the enstatite chondrites the Ru isotope anomalies are not resolved from the terrestrial Ru standard; further work is needed to assess whether enstatite chondrites are distinct from the bulk silicate Earth Ru isotope composition. Our results for primitive chondrites differ from those of a previous study (Chen et al., 2010) in two important aspects. First, for Allende samples decomposed by *AF* we observe smaller Ru isotope anomalies in comparison to those obtained in a previous study employing tabletop digestions (Chen et al., 2010). This could be either due to sample heterogeneity or more likely reflects incomplete digestion of an *s*-process phase in the previous study, meaning that the true Ru isotope anomalies of bulk Allende are slightly smaller than previously observed. Second, for Murchison we observe a ε^{100}Ru deficit, similar to other carbonaceous chondrites, whereas a previous study observed an ε^{100}Ru excess (Chen et al., 2010). This difference probably does not reflect the incomplete dissolution of presolar phases, but may, as argued by Fujii et al. (2006), reflect isotope fractionation by the nuclear field shift effect. Note that our results for Murchison are inconsistent with this effect—because we observe no ε^{104}Ru anomaly in spite of a well-resolved ε^{100}Ru deficit—but are entirely consistent with the expected anomalies for an *s*-deficit.

4.4. Cosmogenic Ru isotopic variations in iron meteorites

Although within-group Ru isotope variations observed for IIAB, IID, IIIAB and IVB iron meteorites (Fig. 4) resemble the variations expected for the heterogeneous distribution of *s*-process Ru, they are unlikely to be nucleosynthetic in origin. This is because iron meteorites belonging to the same chemical group are thought to have formed by fractional crystallization of a single metallic melt, which itself formed by large-scale melting and metal segregation (Scott and Wasson, 1975). Thus, any pre-existing nucleosynthetic isotope variability within the parent body should have been homogenized during melting and core formation.

The within-group variations are most likely attributable to cosmic ray-induced effects, because (1) the largest isotopic shifts in each group are observed for strongly irradiated samples with CRE ages >500 Ma (i.e., Ainsworth, Carbo, Charcas, Tlacotepec) (Fig. 4), and (2) for each group the Ru isotope variations are correlated with the Pt isotope composition of each sample (Fig. 5). Previous studies have shown that the Pt isotope composition of iron meteorites can be modified by cosmic ray-induced neutron capture reactions while nucleosynthetic Pt isotope anomalies are absent (Kruijer et al., 2013a, 2014; Wittig et al., 2013). The Ru-Pt isotope correlations observed for each group of magmatic irons, therefore, suggest that the Ru isotope variations also are of cosmogenic origin.

To assess whether the observed within-group Ru isotope variations are *qualitatively* consistent with an origin by

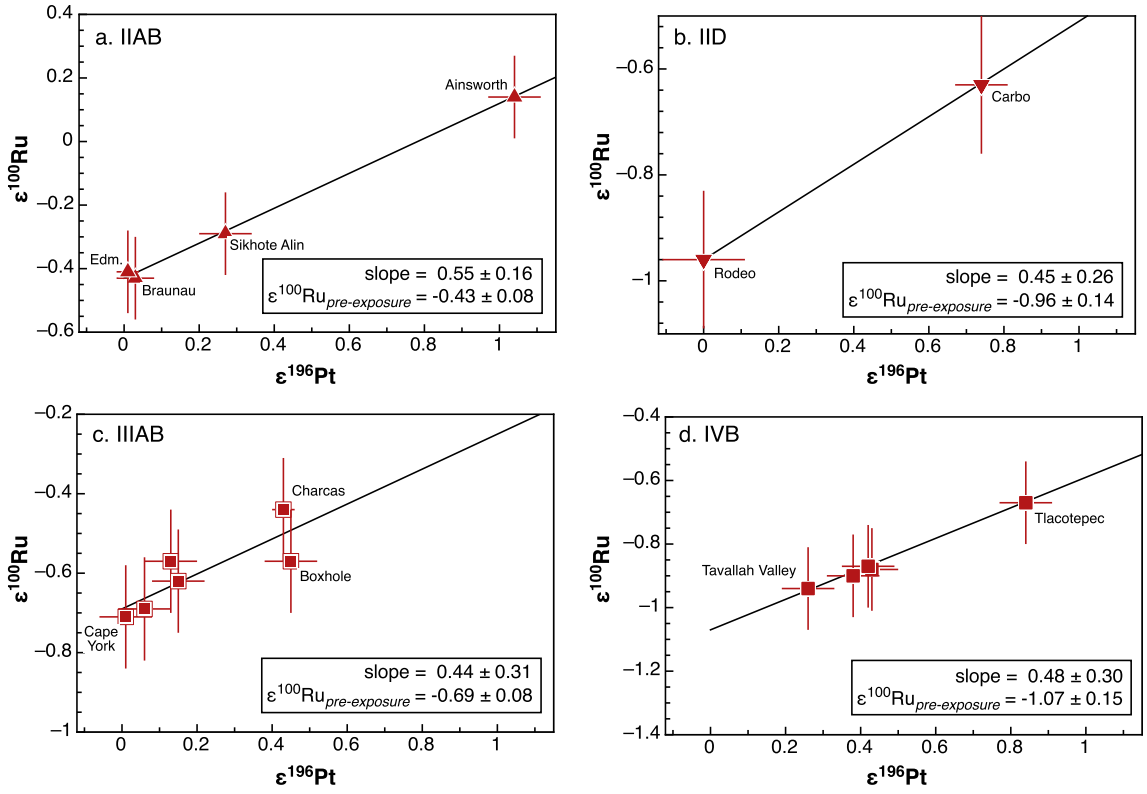

Fig. 5. ε^{100}Ru *vs.* ε^{196}Pt for magmatic iron meteorite groups IIAB (a.), IID (b.), IIIAB (c.) and IVB (d.). Platinum isotope data from Kruijer et al. (2013a, 2014) and Matthes et al. (2015) have been obtained on the same sample digestion solutions or samples that were cut in immediate contact to the location of samples used for Ru isotope data. Combined ε^{100}Ru and ε^{196}Pt data is provided in Table 3. Errors shown for Ru represent the external uncertainty (±0.13 ε-units, 2σ) of our method as defined by replicate analysis of reference samples (Table 1). Solid lines represent linear regressions through the meteorite data calculated using ISOPLOT (Ludwig, 2003), slope and intercept values are given in boxes with 2σ uncertainty. Pre-exposure ε^{100}Ru values are defined by the intersection at the ordinate at ε^{196}Pt = 0.

Table 4
Neutron capture-corrected and representative group averages.

Group	ε^{96}Ru	ε^{98}Ru	ε^{100}Ru	ε^{102}Ru	ε^{104}Ru
Iron meteorites					
IAB[a]	0.06 ± 0.20	0.03 ± 0.29	−0.02 ± 0.06	−0.03 ± 0.04	0.06 ± 0.09
IIAB[b]	0.31 ± 0.28	0.32 ± 0.33	−0.43 ± 0.08	−0.21 ± 0.10	−0.07 ± 0.28
IID[b]	0.35 ± 0.44	0.36 ± 0.51	−0.96 ± 0.14	−0.42 ± 0.15	−0.04 ± 0.31
IIIAB[b]	0.61 ± 0.28	0.41 ± 0.32	−0.69 ± 0.08	−0.24 ± 0.09	0.21 ± 0.19
IVA[a]	0.08 ± 0.14	0.21 ± 0.33	−0.26 ± 0.04	−0.12 ± 0.05	−0.08 ± 0.10
IVB[b]	0.46 ± 0.43	0.14 ± 0.59	−1.07 ± 0.15	−0.32 ± 0.17	0.00 ± 0.28
Chinga[a]	0.22 ± 0.18	0.36 ± 0.71	−1.03 ± 0.04	−0.42 ± 0.10	0.12 ± 0.26
Chondrites					
Ordinary[a]	0.35 ± 0.14	0.14 ± 0.21	−0.30 ± 0.03	−0.12 ± 0.04	0.12 ± 0.16
Enstatite[a]	0.18 ± 0.33	0.13 ± 0.79	−0.10 ± 0.12	−0.08 ± 0.19	0.12 ± 0.13
CV[a]	0.57 ± 0.19	0.52 ± 0.21	−1.01 ± 0.05	−0.38 ± 0.05	0.19 ± 0.10
CM[a]	0.44 ± 0.45	0.51 ± 0.52	−0.93 ± 0.13	−0.33 ± 0.15	0.11 ± 0.31
CB[a]	0.11 ± 0.18	0.26 ± 0.29	−1.04 ± 0.04	−0.45 ± 0.10	−0.08 ± 0.20
CR-an[a]	0.87 ± 0.09	0.38 ± 0.19	−1.15 ± 0.04	−0.50 ± 0.03	0.16 ± 0.09

[a] Calculated group or sample averages from pooled individual measurements of multiple sample digestions. Uncertainties represent 95% confidence intervals for samples measured multiple times ($n \geqslant 4$) or external uncertainties (2s.d.) as stated in Table 1 for $n \leqslant 3$ replicate measurements.

[b] Neutron capture corrected ε^{i}Ru values derived from linear regressions of ε^{i}Ru *vs.* ε^{196}Pt (Fig. 5 and E-Annex Figs. EA4-EA7), uncertainties are 2σ.

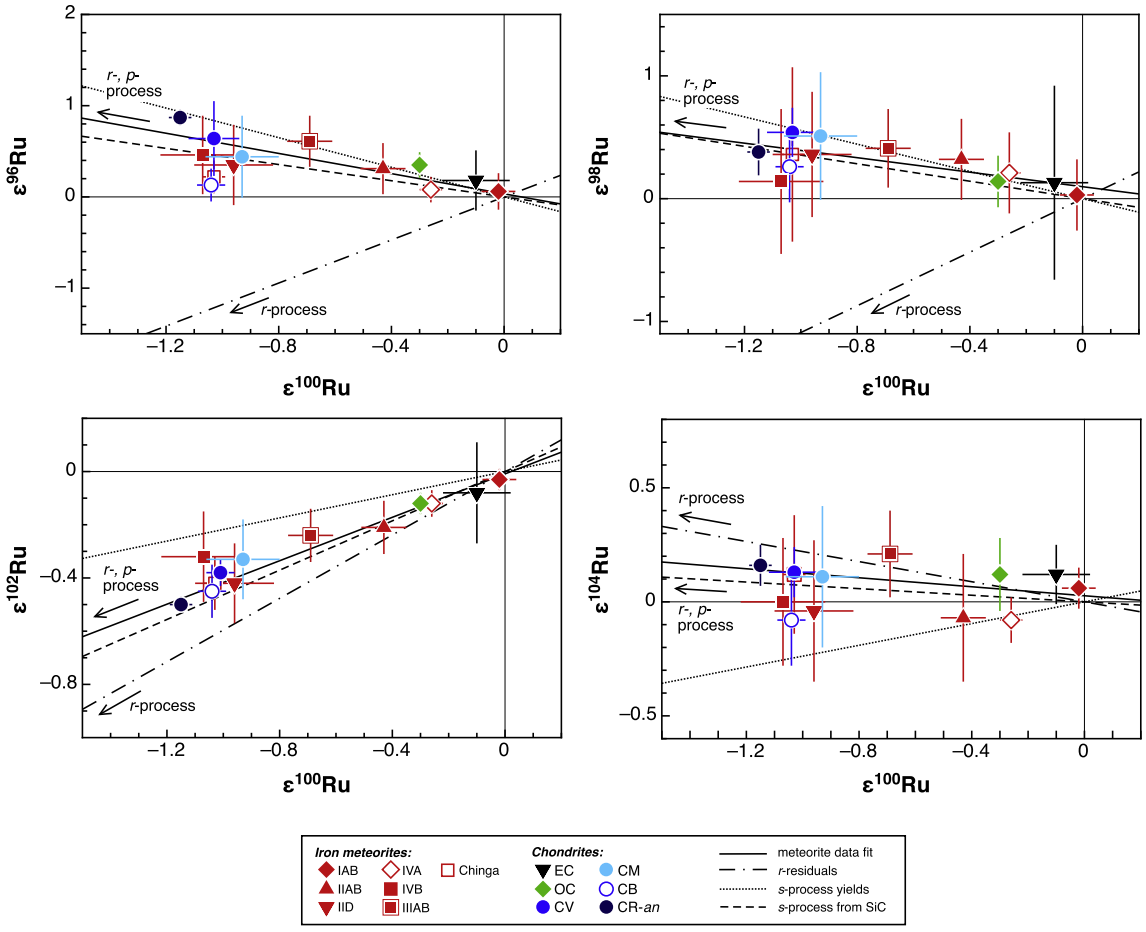

Fig. 6. ε^{i}Ru *vs.* ε^{100}Ru for meteorites in comparison to mixing lines between presumed *s*- and *r*-process components and the terrestrial Ru isotope composition. Solid black lines represent linear regressions of the meteorite data from Table 4 calculated using ISOPLOT (Ludwig, 2003); slopes for ε^{96}Ru (a), ε^{98}Ru (b), ε^{102}Ru (c) and ε^{104}Ru (d) *vs.* ε^{100}Ru are -0.55 ± 0.35, -0.29 ± 0.21, 0.41 ± 0.04, and -0.10 ± 0.13, respectively (Table 5). Broken lines represent mixing lines between terrestrial Ru and an *s*-process component as defined by Ru isotope data for SiC (dashed line, Savina et al., 2004); calculated *s*-process yields (dotted line, Bisterzo et al., 2011) and corresponding *r*-process residuals (dashed-dotted line). All meteorites plot along mixing lines between an *s*-process component as defined by SiC and terrestrial Ru.

Table 5
Summary of ε^{i}Ru *vs.* ε^{100}Ru slopes obtained from Allende leachates, bulk meteorites and presolar SiC.

	ε^{96}Ru *vs.* ε^{100}Ru	ε^{98}Ru *vs.* ε^{100}Ru	ε^{102}Ru *vs.*ε^{100}Ru	ε^{104}Ru *vs.* ε^{100}Ru
Leachates[a]	-0.44 ± 0.09	-0.39 ± 0.18	0.415 ± 0.006	-0.04 ± 0.01
Bulk meteorites[b]	-0.55 ± 0.35	-0.29 ± 0.21	0.41 ± 0.04	-0.10 ± 0.13
SiC[c]	−0.44	−0.36	0.46	−0.07

[a] Slopes from linear regression calculations for Allende leachate data (Table 2, Fig. 2).
[b] Slopes from linear regression calculations for meteorite data (Table 4, Fig. 6).
[c] Slopes from Ru isotope data for SiC grains from Savina et al. (2004).

neutron capture, we used the model of Nyquist et al. (1995) to calculate the relative magnitude and direction of cosmic ray-induced modifications on Ru isotope ratios. Because neutron capture effects in iron meteoroids are dominated by reactions occurring at epithermal energies (>0.5 eV) (Kruijer et al., 2013b; Leya and Masarik, 2013), the resonance integrals (RI) rather than the thermal cross sections govern the relative effects of neutron capture on Ru isotopes (cross-sections and resonance integrals were obtained from the ENDFB-VI.8 300 K or JEFF-3.2 libraries at https://www-nds.iaea.org/exfor/endf.htm and are summarized in Tables EA1 and EA2). As ^{99}Ru (RI ~137 barns) and ^{101}Ru (RI ~111 barns) have by far the highest resonance integrals, the reactions ^{99}Ru(n,γ)^{100}Ru and ^{101}Ru(n,γ)^{102}Ru dominate the overall neutron capture effects on Ru isotopes in iron meteorites. As a consequence, the ^{99}Ru/^{101}Ru ratio, which is used for instrumental mass bias correction, is modified leading to isotope shifts through

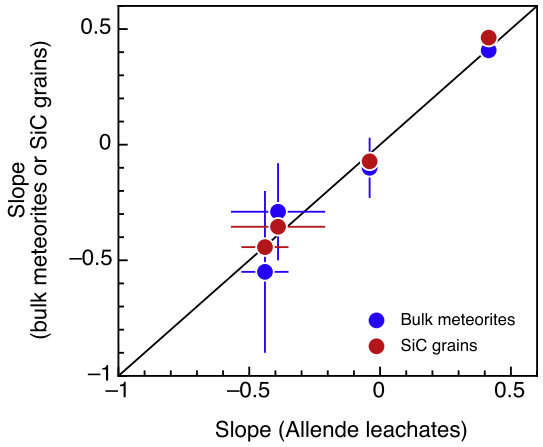

Fig. 7. Comparison of slopes obtained from linear regression of Ru isotope data for Allende leachates (Fig. 2), bulk meteorites (Fig. 6) and slopes observed for mainstream SiC grains (Savina et al., 2004). Linear regressions for Allende leachates and bulk meteorites were calculated using ISOPLOT (Ludwig, 2003). Uncertainties are 2σ. A summary of the slopes is given in Table 5.

normalization to the terrestrial $^{99}Ru/^{101}Ru$. In addition, all $^{i}Ru/^{101}Ru$ ratios increase due to the consumption of ^{101}Ru during neutron capture, resulting in a small increase in all $\varepsilon^{i}Ru$ values. The largest increase occurs for $\varepsilon^{100}Ru$ and $\varepsilon^{102}Ru$, because the neutron capture reactions mainly produce ^{100}Ru and ^{102}Ru. The results of the model calculations are at least qualitatively consistent with the observed within-group Ru isotope variations, because more positive $\varepsilon^{i}Ru$ values are observed for the most strongly irradiated samples of each group.

The cosmogenic Ru isotope variations can be corrected using the $\varepsilon^{i}Ru$-$\varepsilon^{196}Pt$ correlations obtained for each group of irons, with the intercept at $\varepsilon^{196}Pt = 0$ defining the pre-exposure $\varepsilon^{i}Ru$ (i.e., unaffected by neutron capture) for each group (Fig. 5). Owing to the depth dependence of neutron capture effects, correlated cosmogenic Ru and Pt isotope anomalies are only expected for the same or adjacent sample pieces of a given iron meteorite. This condition is met for the iron meteorite samples investigated in the present study, by either using the same digestion solution or samples that were cut in immediate contact to the location of the samples used for our previous Pt isotope studies (Kruijer et al., 2013a, 2014; Matthes et al., 2014, 2015) (Table 3). For groups IIAB, IID, IIIAB and IVB well-defined $\varepsilon^{100}Ru$-$\varepsilon^{196}Pt$ correlations are obtained (Fig. 5). The slopes of these correlation lines all agree within their uncertainties, with an average slope of 0.48 ± 0.12 (2s.d.). The pre-exposure $\varepsilon^{100}Ru$ values obtained from linear regressions of the Ru and Pt isotope data vary from -0.43 ± 0.08 for the IIAB irons to -1.07 ± 0.15 for the IVB irons (Fig. 5). Note that the IVA irons investigated in this study (Gibeon and Muonionalusta) show no resolved Pt isotope anomalies and that, therefore, their mean $\varepsilon^{100}Ru = -0.26 \pm 0.04$ requires no correction for cosmogenic effects. No corrections could be made for the IAB iron meteorites, because no Pt isotope data are available for these samples. The pre-exposure $\varepsilon^{100}Ru$ for the IAB irons could, therefore, be slightly lower than the measured value of $\varepsilon^{100}Ru \sim 0$ (Table 4).

While the neutron capture effects on $\varepsilon^{100}Ru$ are clearly resolved, cosmogenic variations in other Ru isotope ratios are less significant and well-defined correlations between $\varepsilon^{196}Pt$ and $\varepsilon^{96}Ru$, $\varepsilon^{98}Ru$, $\varepsilon^{102}Ru$ or $\varepsilon^{104}Ru$ are only obtained for the IIAB iron meteorites. This is because cosmogenic variations on $\varepsilon^{96}Ru$, $\varepsilon^{98}Ru$, $\varepsilon^{102}Ru$ or $\varepsilon^{104}Ru$ are mostly within the analytical uncertainty of the Ru isotope measurements (E-annex, Figs. EA4–EA7). It is nevertheless important to correct for the cosmogenic effects, because these may still be significant if only irradiated samples are investigated (such as for the IVB irons). The pre-exposure Ru isotope compositions of the different groups of iron meteorites, obtained from linear regressions of $\varepsilon^{i}Ru$ *vs.* $\varepsilon^{196}Pt$ for each group, are summarized in Table 4.

4.5. Mo–Ru isotope correlation

The iron meteorites (corrected for cosmogenic effects) and bulk chondrites display correlated Ru isotope anomalies, and as the leachates, plot on mixing lines between terrestrial Ru and an *s*-process component with a composition as measured in presolar SiC grains (Fig. 6). The slopes of these mixing lines obtained from the linear regression of the Allende leachate and bulk meteorite data agree very well and also agree with the slopes calculated using the *s*-process composition as measured in SiC grains (Table 5, Fig. 7). The correlated Ru isotope anomalies of both the bulk meteorites and the Allende leachates, therefore, can be attributed to the heterogeneous distribution of the same presolar *s*-process enriched component.

Insights into the nature and origin of this presolar component can be obtained from the assessment of collateral effects on the isotope composition of other elements. Dauphas et al. (2004) and Burkhardt et al. (2011) observed that nucleosynthetic $\varepsilon^{92}Mo$ and $\varepsilon^{100}Ru$ isotope anomalies in iron meteorites and the CV chondrite Allende correlate as predicted from *s*-process nucleosynthesis theory and may, therefore, reflect the heterogeneous distribution of a common *s*-process carrier. However, we find that several samples and in particular the carbonaceous chondrites deviate from the Mo–Ru isotope correlation line (Fig. 8). While enstatite and ordinary chondrites together with the IAB, IIAB, IIIAB and IVA iron meteorites exhibit correlated Mo and Ru isotope anomalies, carbonaceous chondrites (CM, CV, CB), Tafassasset and the IID and IVB irons define a horizontal array in the $\varepsilon^{92}Mo$-$\varepsilon^{100}Ru$ plot; these samples display very similar Ru but different Mo isotope anomalies (Fig. 8).

There are three possible reasons why some samples plot off the Mo–Ru correlation. First, among the samples plotting slightly off the Mo–Ru correlation line are two iron meteorite groups having significant neutron capture effects (IID, IVB). These effects have been corrected for Ru in the present study, but not for Mo. Thus, the IID and IVB irons might plot off the correlation line because of unaccounted cosmic ray effects on Mo isotopes. However, the Mo isotope anomalies reported by Burkhardt et al.

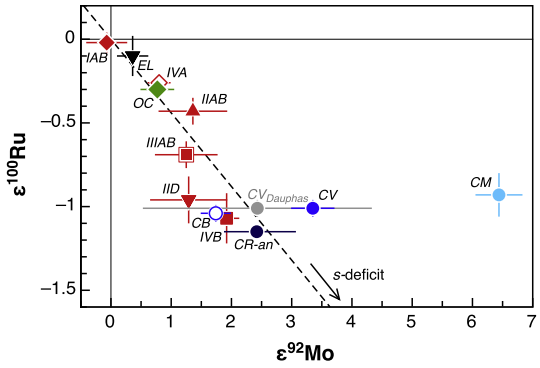

Fig. 8. ε^{100}Ru *vs.* ε^{92}Mo for bulk meteorites. Molybdenum isotope data are from Burkhardt et al. (2011) and in case of Allende ($CV_{Dauphas}$) from Dauphas et al. (2002a,b). Dashed line represents a mixing line calculated between a presumed *s*-process Mo and Ru component as deduced from SiC data (Nicolussi et al., 1998; Savina et al., 2004) and terrestrial Mo and Ru isotope compositions. The Ru and Mo isotope data for the meteorites show a dichotomous distribution. Ordinary and enstatite chondrites as well as some iron meteorite groups plot on the *s*-process mixing line, whereas some magmatic iron meteorite groups (e.g. IID) and carbonaceous chondrites (CV, CM, CB) significantly deviate from the mixing line. Ruthenium isotope data and uncertainties for group averages as listed in Table 4. Note that data for IIAB, IID, IIIAB and IVB irons have been corrected for neutron capture effects (as discussed in text, Section 4.4.). Molybdenum isotope data for group averages of IIAB, IIIAB and IVB iron meteorites from Burkhardt et al. (2011) are shown with standard deviation (2s.d.) uncertainty, all other group averages with uncertainties as reported in the original work. Because of the range of ε^{92}Mo anomalies reported for Allende (as discussed in Section 4.5) Mo isotope data from Dauphas et al. (2002a,b) are plotted as an average with standard deviation uncertainty (2s.d.).

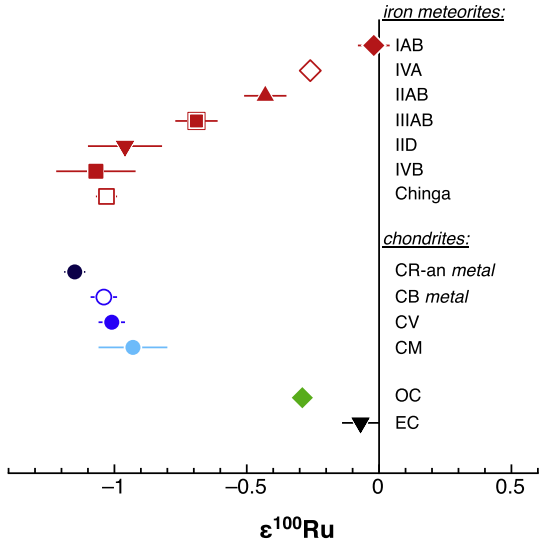

Fig. 9. ε^{100}Ru data for iron meteorites and chondrites.

(2011) for various IVB irons are relatively homogenous, such that at this point only small Mo corrections might be expected. To assess this issue in more detail, combined high-precision Mo, Ru and Pt isotope measurements on the same suite of irons are needed. Either way, carbonaceous chondrites have much younger CRE ages than iron meteorites and so cosmic ray-effects cannot be the sole cause of the deviation of samples from the Mo–Ru correlation line. Second, because the Mo and Ru isotope data were not obtained on the same carbonaceous chondrite sample solution [note that the Mo isotope data plotted in Fig. 8 are from Burkhardt et al. (2011) and were obtained on different samples as the Ru isotope data in the present study], the deviation of carbonaceous chondrites from the Mo–Ru correlation could in principle reflect sample heterogeneity. We note, however, that all carbonaceous chondrites investigated in this study display very similar Ru isotope anomalies, which is an unlikely outcome if significant Ru isotope heterogeneities would exist at the sampling scale. For Mo the situation is less clear, however, because large Mo isotope variations exist among different carbonaceous chondrites (Burkhardt et al., 2011) and perhaps even between different splits of a given carbonaceous chondrite. For instance, for Allende ε^{92}Mo anomalies ranging from ~3.4 (Burkhardt et al., 2011), between ~1.2 and ~3.5 (Dauphas et al., 2002a,b), and ~0.8 (Becker and Walker, 2003) have been reported. The origin of these variations is unclear at present, but given that Allende contains abundant CAI—some of which display large Mo isotope anomalies of up to ~20 ε^{92}Mo (Burkhardt et al., 2011)—it is possible that they reflect sample heterogeneity. In this case it would be difficult to determine the true Mo isotopic composition of bulk Allende and it would also be difficult to assess whether bulk Allende (or other CV chondrites) plots on the Mo-Ru correlation line. Cleary, combined Mo and Ru isotopic data on the very same samples and ideally on aliquots of the same sample solution are needed to address this issue.

The third possible reason why some samples plot off the Mo–Ru correlation line is that this is the result of nebular or parent body processes on presolar phases (Burkhardt et al., 2012a). Because the carbonaceous chondrites display near-constant Ru isotope anomalies (ε^{100}Ru ~ –1) although they have variable Mo isotope compositions (ε^{92}Mo ranging from ~1.7 to ~6.4; Burkhardt et al., 2011), one possibility is that nebular or parent body processes acting on presolar components in carbonaceous chondrites resulted in the release and preferential loss of isotopically anomalous Mo, imparting Mo isotopic heterogeneity on an initially more homogeneous reservoir. It is noteworthy that the CM chondrite Murchison plots furthest away from the Mo-Ru correlation line and has formed under more oxidized conditions than most other chondrites. Thus, one possibility is that these conditions facilitated the formation of volatile Mo oxides, which may have been partly lost. If the removed Mo was isotopically anomalous—because it was partly released from presolar components—then the remaining Mo would display an isotope composition which is complementary to that of the removed Mo (Burkhardt et al., 2012a). Since Mo forms volatile oxides much more readily than Ru (Fegley and Palme, 1985), this process could impart Mo isotope heterogeneity without significantly affecting the Ru isotope composition. This would also be consistent with the light Mo stable isotope composition of CM chondrites compared

to other chondrites, which might reflect the loss of isotopically light Mo oxides during nebular processes (Burkhardt et al., 2014).

Clearly, more work is needed to assess the significance of any deviation of bulk meteorites from the Mo-Ru correlation line. Most of all this will require combined Mo and Ru isotope analyses on the same solution aliquots, especially in the case of primitive chondrites. Moreover, to assess the potential effect of nebular and parent body processes on Mo and Ru isotopes, a comprehensive set of samples formed under different nebular conditions as well as samples characterized by different degrees of parent body alteration must be analyzed. If such analyses would verify that (some) carbonaceous chondrites plot off the Mo-Ru correlation line, then this would be one of the most direct evidence that secondary processes imparted isotopic heterogeneity on an initially more homogeneous reservoir. Obtaining such data would, therefore, be an important task for future studies.

4.6. Implications for the late veneer

The Ru isotope data provide constraints on the source of bodies that may have accreted to the Earth as a late veneer after the completion of core formation. Previous studies have used Os isotope data, relative highly siderophile element (HSE) and chalcogen element abundances to constrain the composition of the late veneer (Brandon et al., 2000, 2006; Meisel et al., 2001; Walker et al., 2002; Horan et al., 2003; Becker et al., 2006; Fischer-Gödde et al., 2010, 2011). Collectively, these studies show that no group of meteorites can account for all the chemical characteristics of the late-accreted material. For instance, whereas Os isotope systematics are most consistent with a ordinary- or enstatite chondrite-like late veneer, relative abundances of Se, Te and S suggest a carbonaceous chondrite-like composition (Wang and Becker, 2013). In addition, superchondritic Pd/Ir and Ru/Ir ratios of the Earth's primitive upper mantle are not easily explained by a late veneer composed entirely of known groups of chondrites (Becker et al., 2006). One possibility to account for these observations would be that the late veneer predominantly consists of carbonaceous chondrite-like material with a minor proportion of differentiated, iron meteorite-like material (Fischer-Gödde and Becker, 2012; Wang and Becker, 2013).

The Ru isotope systematics of meteorites can shed new light on the origin of the late veneer and can potentially be used to identify a genetic link between the late veneer and specific groups of meteorites. Almost the entire Ru in Earth's mantle is thought to derive from the late veneer, and thus only meteorites (or a combination thereof) having a terrestrial Ru isotope composition (i.e., $\varepsilon^{100}Ru \sim 0$) are potential sources of the late veneer (Dauphas et al., 2004). However, all meteorites investigated in the present study (except possibly the IAB irons and enstatite chondrites) exhibit nucleosynthetic Ru isotope anomalies and, therefore, cannot be the source of the late veneer (Fig. 9). Moreover, since all meteorites are characterized by a deficit in *s*-process Ru relative to the Earth's mantle, a combination of different meteorites also does not yield the terrestrial Ru isotope composition. Only the IAB irons and the EL chondrites show no clearly resolved Ru isotope anomalies, but the chemical composition of these meteorite groups makes them unlikely sources of the late veneer. Combined, these results suggest that no group of meteorites nor a combination thereof are viable sources of the late veneer. However, a more detailed study of Ru isotopes in a more comprehensive set of chondrites is needed to thoroughly assess the role of known meteorites as potential sources of the late veneer. If, in analogy to Mo, all carbonaceous chondrites were characterized by a deficit in *s*-process Ru compared to the Earth's mantle, then the late veneer must derive from a population of bodies distinct from the meteorite parent bodies. One possibility would then be that the late veneer derived from material in the inner solar system, similar to the material constituting the main building blocks of the Earth.

5. CONCLUSIONS

Correlated Ru isotope anomalies in iron meteorites and bulk ordinary, enstatite and carbonaceous chondrites reflect variable deficits in *s*-process Ru in meteorite parent bodies compared to the Earth. While the Ru isotope data are consistent with widespread *s*-process heterogeneity, not all the Ru isotope anomalies are caused by variable abundances of presolar components. Our new combined Ru and Pt isotope data for iron meteorites show that secondary neutron capture resulting from cosmic ray exposure can also lead to Ru isotope shifts, and that the magnitude of these shifts can be quantified by measuring Pt isotopes in the same sample. After correction of cosmic ray effects, the remaining Ru isotope anomalies in iron meteorites are of nucleosynthetic origin and indicate variable deficits in *s*-process Ru in iron meteorite parent bodies. For primitive chondrites neutron capture effects on Ru isotopes are insignificant, given their much shorter cosmic ray exposure times compared to iron meteorites. However, the interpretation of Ru isotope data of chondrites can be compromised by incomplete digestion of acid-resistant presolar phases, as demonstrated here for the chondrites Allende and Murchison. Employing a complete digestion technique is, therefore, mandatory for Ru isotope analyses of primitive chondrites, as previously demonstrated for Os (Brandon et al., 2005; Yokoyama et al., 2007).

Large internal Ru isotope variations in the Allende chondrite (CV3) reflect variable proportions of *s*-process Ru in the individual leach fractions, with an isotopic composition as measured in presolar SiC grains. Because the *s*-process Ru is already released by relatively mild leaching with HF, it probably does not reside in SiC grains, but either is hosted in an unidentified, acid-soluble presolar carrier or has been released from more resistant carriers (e.g., SiC) and incorporated into more soluble phases by parent body or nebular processes. Either way, the same carrier (or one with the same *s*-process composition) is heterogeneously distributed at the bulk planetary scale, as is evident from the observation that in $\varepsilon^{i}Ru$-$\varepsilon^{100}Ru$ plots all bulk meteorites as well as the Earth's mantle fall on the mixing lines defined by the Allende leachates.

Our new Ru isotope data confirm that ordinary and enstatite chondrites as well as most iron meteorites exhibit correlated Ru and Mo isotope anomalies, consistent with the heterogeneous distribution of a common *s*-process carrier (Dauphas et al., 2004; Burkhardt et al., 2011). However, some carbonaceous chondrites and possibly also some iron meteorites (IID+IVB) appear to deviate from the Ru–Mo correlation line. This may reflect unaccounted cosmic ray-induced effects on Mo isotopes in iron meteorites, sample heterogeneity caused by the presence of chondrite components with large Mo and Ru isotope anomalies in carbonaceous chondrites, or solar nebula and/or parent-body processes that acted to modify the initial population of presolar components in (at least some) carbonaceous chondrites. Distinguishing between these possibilities will require combined Mo and Ru isotope data for meteorites obtained for the same sample solution.

The Ru isotope results indicate that meteorites do not appear to represent the material delivered to the Earth's mantle as a late veneer, but additional analyses of a more comprehensive suite of especially carbonaceous chondrites are necessary to firmly arrive at this conclusion. If confirmed by future studies, then the late veneer must derive from a different population of small bodies than known meteorites and in this case might simply represent the material left over from the main stages of terrestrial planet formation.

ACKNOWLEDGEMENTS

We thank C. Smith (Natural History Museum, London), J. Zipfel (Senckenbergmuseum, Frankfurt), D. Ebel (American Museum of National History, New York), P. Heck (Field Museum, Chicago), T. McCoy (Smithsonian Institution, Washington), F. Brandstätter (Naturhistorisches Museum Wien), C. Herd (Univ. Alberta, Edmonton), R. Wieler (ETH Zürich) and A. Bischoff for providing samples and U. Heitmann for technical support. Thanks to B. O'Driscoll and K. Bermingham for providing the chromitite sample from the Shetland Ophiolite. Reviews from three anonymous reviewers and comments from associate editor F. Moynier helped to improve the manuscript and are gratefully acknowledged.

APPENDIX A. SUPPLEMENTARY DATA

Supplementary data associated with this article can be found, in the online version, at http://dx.doi.org/10.1016/j.gca.2015.07.032.

REFERENCES

Akram W., Schönbächler M., Bisterzo S. and Gallino R. (2015) Zirconium isotope evidence for the heterogeneous distribution of *s*-process materials in the solar system. *Geochim. Cosmochim. Acta* **165**, 484–500.

Amari S., Hoppe P., Zinner E. and Lewis R. S. (1995) Trace-element concentrations in single circumstellar silicon carbide grains from the Murchison meteorite. *Meteoritics* **30**, 679–693.

Arlandini C., Käppeler F. and Wisshak K. (1999) Neutron capture in low-mass asymptotic giant branch stars: cross sections and abundance signatures. *Astrophys. J.* **525**, 886–900.

Becker H. and Walker R. J. (2003) In search of extant Tc in the early solar system: ^{98}Ru and ^{99}Ru abundances in iron meteorites and chondrites. *Chem. Geol.* **196**, 43–56.

Becker H., Dalpe C. and Walker R. J. (2002) High-precision Ru isotopic measurements by multi-collector ICP-MS. *Analyst* **127**, 775–780.

Becker H., Horan M. F., Walker R. J., Gao S., Lorand J. P. and Rudnick R. L. (2006) Highly siderophile element composition of the Earth's primitive upper mantle: constraints from new data on peridotite massifs and xenoliths. *Geochim. Cosmochim. Acta* **70**, 4528–4550.

Bisterzo S., Gallino R., Straniero O., Cristallo S. and Käppeler F. (2011) The *s*-process in low-metallicity stars – II. Interpretation of high-resolution spectroscopic observations with asymptotic giant branch models. *Mon. Not. R. Astron. Soc.* **418**, 284–319.

Brandon A. D., Snow J. E., Walker R. J., Morgan J. W. and Mock T. D. (2000) ^{190}Pt–^{186}Os and ^{187}Re–^{187}Os systematics of abyssal peridotites. *Earth Planet. Sci. Lett.* **177**, 319–335.

Brandon A. D., Humayun M., Puchtel I. S., Leya I. and Zolensky M. (2005) Osmium Isotope evidence for an *s*-process carrier in primitive chondrites. *Science* **309**, 1233–1236.

Brandon A. D., Walker R. J. and Puchtel I. S. (2006) Platinum-osmium isotope evolution of the Earth's mantle: constraints from chondrites and Os-rich alloys. *Geochim. Cosmochim. Acta* **70**, 2093–2103.

Brennecka G. A., Borg L. E. and Wadhwa M. (2013) Evidence for supernova injection into the solar nebula and the decoupling of *r*-process nucleosynthesis. *Proc. Natl. Acad. Sci.* **110**, 17241–17246.

Burkhardt C., Kleine T., Oberli F., Pack A., Bourdon B. and Wieler R. (2011) Molybdenum isotope anomalies in meteorites: constraints on solar nebula evolution and origin of the Earth. *Earth Planet. Sci. Lett.* **312**, 390–400.

Burkhardt C., Kleine T., Dauphas N. and Wieler R. (2012a) Origin of isotopic heterogeneity in the solar nebula by thermal processing and mixing of nebular dust. *Earth Planet. Sci. Lett.* **357–358**, 298–307.

Burkhardt C., Kleine T., Dauphas N. and Wieler R. (2012b) Nucleosynthetic tungsten isotope anomalies in acid leachates of the Murchison chondrite: implications for Hf-W chronometry. *Astrophys. J. Lett.* **753**, L6.

Burkhardt C., Hin R. C., Kleine T. and Bourdon B. (2014) Evidence for Mo isotope fractionation in the solar nebula and during planetary differentiation. *Earth Planet. Sci. Lett.* **391**, 201–211.

Chen J. H., Papanastassiou D. A. and Wasserburg G. J. (2010) Ruthenium endemic isotope effects in chondrites and differentiated meteorites. *Geochim. Cosmochim. Acta* **74**, 3851–3862.

Chou C. L. (1978) Fractionation of siderophile elements in the Earth's upper mantle. *Proc. Lunar Planet. Sci. Conf.* **9**, 219–230.

Dauphas N., Marty B. and Reisberg L. (2002a) Molybdenum evidence for inherited planetary scale isotope heterogeneity of the protosolar nebula. *Astrophys. J.* **565**, 640–644.

Dauphas N., Marty B. and Reisberg L. (2002b) Molybdenum nucleosynthetic dichotomy revealed in primitive meteorites. *Astroph. J.* **569**, L139–L142.

Dauphas N., Davis A. M., Marty B. and Reisberg L. (2004) The cosmic molybdenum-ruthenium isotope correlation. *Earth Planet. Sci. Lett.* **226**, 465–475.

Dauphas N., Remusat L., Chen J. H., Roskosz M., Papanastassiou D. A., Stodolna J., Guan Y., Ma C. and Eiler J. M. (2010) Neutron-rich chromium isotope anomalies in supernova nanoparticles. *Astrophys. J.* **720**, 1577–1591.

Fegley B. and Palme H. (1985) Evidence for oxidizing conditions in the solar nebula from Mo and W depletions in refractory inclusions in carbonaceous chondrites. *Earth Planet. Sci. Lett.* **72**, 311–326.

Fischer-Gödde M. and Becker H. (2012) Osmium isotope and highly siderophile element constraints on ages and nature of meteoritic components in ancient lunar impact rocks. *Geochim. Cosmochim. Acta* **77**, 135–156.

Fischer-Gödde M., Becker H. and Wombacher F. (2010) Rhodium, gold and other highly siderophile element abundances in chondritic meteorites. *Geochim. Cosmochim. Acta* **74**, 356–379.

Fischer-Gödde M., Becker H. and Wombacher F. (2011) Rhodium, gold and other highly siderophile elements in orogenic peridotites and peridotite xenoliths. *Chem. Geol.* **280**, 365–383.

Fujii T., Moynier F., Telouk P. and Albarede F. (2006) Mass-independent isotope fractionation of molybdenum and ruthenium and the origin of isotopic anomalies in Murchison. *Astrophys. J.* **647**, 1506–1516.

Horan M. F., Walker R. J., Morgan J. W., Grossman J. N. and Rubin A. E. (2003) Highly siderophile elements in chondrites. *Chem. Geol.* **196**, 5–20.

Huss G. R. and Lewis R. S. (1995) Presolar diamond, SiC, and graphite in primitive chondrites - abundances as a function of meteorite class and petrologic type. *Geochim. Cosmochim. Acta* **59**, 115–160.

Kimura K., Lewis R. S. and Anders E. (1974) Distribution of gold and rhenium between nickel-iron and silicate melts – implications for abundance of siderophile elements on Earth and Moon. *Geochim. Cosmochim. Acta* **38**, 683–701.

Kruijer T. S., Sprung P., Kleine T., Leya I., Burkhardt C. and Wieler R. (2012) Hf-W chronometry of core formation in planetesimals inferred from weakly irradiated iron meteorites. *Geochim. Cosmochim. Acta* **99**, 287–304.

Kruijer T. S., Fischer-Gödde M., Kleine T., Sprung P., Leya I. and Wieler R. (2013a) Neutron capture on Pt isotopes in iron meteorites and the Hf-W chronology of core formation in planetesimals. *Earth Planet. Sci. Lett.* **361**, 162–172.

Kruijer T. S., Sprung P., Kleine T., Leya I. and Wieler R. (2013b) The abundance and isotopic composition of Cd in iron meteorites. *Meteorit. Planet. Sci.* **48**, 2597–2607.

Kruijer T. S., Touboul M., Fischer-Gödde M., Bermingham K. R., Walker R. J. and Kleine T. (2014) Protracted core formation and rapid accretion of protoplanets. *Science* **344**, 1150–1154.

Leya I. and Masarik J. (2013) Thermal neutron capture effects in radioactive and stable nuclide systems. *Meteorit. Planet. Sci.* **48**, 665–685.

Leya I., Schonbachler M., Wiechert U., Krahenbuhl U. and Halliday A. N. (2008) Titanium isotopes and the radial heterogeneity of the solar system. *Earth Planet. Sci. Lett.* **266**, 233–244.

Ludwig K. R. (2003) ISOPLOT 3.00. A geochronological toolkit for Mikrosoft Excel. Berkeley Geochronological Center Spec. Publ. No. 4, 70 pp.

Matthes M., Fischer-Gödde M., Kruijer T. S., Laeya I. and Kleine T. (2014) Rapid cooling of the IIIAB iron meteorite parent body inferred from Pd-Ag chronometry. *Lunar Planet. Sci. Conf. XXXXV*, #2197.

Matthes M., Fischer-Gödde M., Kruijer T. S., Leya I., Kleine T. (2015) Correction of neutron capture-effects on Ag isotopes with application to the Pd-Ag isotope chronometry of iron meteorites. Geochim. Cosmochim. Acta (in press).

Meisel T., Walker R. J., Irving A. J. and Lorand J.-P. (2001) Osmium isotopic compositions of mantle xenoliths: a global perspective. *Geochim. Cosmochim. Acta* **65**, 1311–1323.

Morgan J. W. and Walker R. J. (1989) Isotopic determinations of rhenium and osmium in meteorites by using fusion, distillation and ion exchange separations. *Anal. Chim. Acta* **222**, 291–300.

Nicolussi G. K., Pellin M. J., Davis A. M., Amari S. and Clayton R. N. (1998) Molybdenum isotopic composition of individual presolar silicon carbide grains from the Murchison meteorite. *Geochim. Cosmochim. Acta* **62**, 1093–1104.

Nyquist L. E., Wiesmann H., Bansal B., Shih C. Y., Keith J. E. and Harper C. L. (1995) ^{146}Sm–^{142}Nd formation interval for the lunar mantle. *Geochim. Cosmochim. Acta* **59**, 2817–2837.

O'Driscoll B., Day J. M. D., Walker R. J., Daly J. S., McDonough W. F. and Piccoli P. M. (2012) Chemical heterogeneity in the upper mantle recorded by peridotites and chromitites from the Shetland Ophiolite Complex Scotland. *Earth Planet. Sci. Lett.* **333–334**, 226–237.

Qin L. P., Dauphas N., Wadhwa M., Markowski A., Gallino R., Janney P. E. and Bouman C. (2008) Tungsten nuclear anomalies in planetesimal cores. *Astrophys. J.* **674**, 1234–1241.

Qin L., Nittler L. R., Alexander C. M. O. D., Wang J., Stadermann F. J. and Carlson R. W. (2011) Extreme ^{54}Cr-rich nano-oxides in the CI chondrite Orgueil – implication for a late supernova injection into the solar system. *Geochim. Cosmochim. Acta* **75**, 629–644.

Regelous M., Elliott T. and Coath C. D. (2008) Nickel isotope heterogeneity in the early Solar System. *Earth Planet. Sci. Lett.* **272**, 330–338.

Reisberg L., Dauphas N., Luguet A., Pearson D. G., Gallino R. and Zimmermann C. (2009) Nucleosynthetic osmium isotope anomalies in acid leachates of the Murchison meteorite. *Earth Planet. Sci. Lett.* **277**, 334–344.

Roy-Barman M. (1993) Mesure du rapport ^{187}Os/^{186}Os dans les basalts et les péridotites: Contribution à la systématique ^{187}Re-^{187}Os dans le manteau. Ph.D. University of Paris.

Savina M. R., Davis A. M., Tripa C. E., Pellin M. J., Gallino R., Lewis R. S. and Amari S. (2004) Extinct technetium in silicon carbide stardust grains: implications for stellar nucleosynthesis. *Science* **303**, 649–652.

Scott E. R. D. and Wasson J. T. (1975) Classification and properties of iron meteorites. *Rev. Geophys. Space Phys.* **13**, 527–546.

Shirey S. B. and Walker R. J. (1995) Carius tube digestion for low-blank Rhenium-Osmium analysis. *Anal. Chem.* **67**, 2136–2141.

Steele R. C. J., Elliott T., Coath C. D. and Regelous M. (2011) Confirmation of mass-independent Ni isotopic variability in iron meteorites. *Geochim. Cosmochim. Acta* **75**, 7906–7925.

Trinquier A., Birck J. L. and Allègre C. J. (2007) Widespread ^{54}Cr heterogeneity in the inner solar system. *Astrophys. J.* **655**, 1179–1185.

Trinquier A., Elliott T., Ulfbeck D., Coath C., Krot A. N. and Bizzarro M. (2009) Origin of nucleosynthetic isotope heterogeneity in the solar protoplanetary disk. *Science* **324**, 374–376.

van Acken D., Brandon A. D. and Humayun M. (2011) High-precision osmium isotopes in enstatite and Rumuruti chondrites. *Geochim. Cosmochim. Acta* **75**, 4020–4036.

Voshage H. and Feldmann H. (1979) Investigations on cosmic-ray-produced nuclides in iron meteorites, 3. Exposure ages, meteoroid sizes and sample depths determined by mass spectrometric analyses of potassium and rare gases. *Earth Planet. Sci. Lett.* **45**, 293–308.

Walker R. J. (2012) Evidence for homogeneous distribution of osmium in the protosolar nebula. *Earth Planet. Sci. Lett.* **351–352**, 36–44.

Walker R. J., Horan M. F., Morgan J. W., Becker H., Grossman J. N. and Rubin A. E. (2002) Comparative ^{187}Re–^{187}Os systematics of chondrites: implications regarding early solar system processes. *Geochim. Cosmochim. Acta* **66**, 4187–4201.

Wang Z. and Becker H. (2013) Ratios of S, Se and Te in the silicate Earth require a volatile-rich late veneer. *Nature* **499**, 328–331.

Westland A. D. and Beamish F. E. (1954) Study of Osmium and Ruthenium distillations. *Anal. Chem.* **26**, 739–741.

Wittig N., Humayun M., Brandon A. D., Huang S. and Leya I. (2013) Coupled W-Os–Pt isotope systematics in IVB iron meteorites: in situ neutron dosimetry for W isotope chronology. *Earth Planet. Sci. Lett.* **361**, 152–161.

Yokoyama T., Rai V. K., Alexander M. O., Lewis R. S., Carlson R. W., Shirey S. B., ThiernenS M. H. and Walker R. J. (2007) Osmium isotope evidence for uniform distribution of *s*- and *r*-process components in the early solar system. *Earth Planet. Sci. Lett.* **259**, 567–580.

Yokoyama T., Alexander C. M. O. and Walker R. J. (2010) Osmium isotope anomalies in chondrites: results for acid residues and related leachates. *Earth Planet. Sci. Lett.* **291**, 48–59.

Young E. D., Galy A. and Nagahara H. (2002) Kinetic and equilibrium mass-dependent isotope fractionation laws in nature and their geochemical and cosmochemical significance. *Geochim. Cosmochim. Acta* **66**, 1095–1104.

Zhang J. J., Dauphas N., Davis A. M. and Pourmand A. (2011) A new method for MC-ICPMS measurement of titanium isotopic composition: identification of correlated isotope anomalies in meteorites. *J. Anal. At. Spectrom.* **26**, 2197–2205.

Associate editor: Frederic Moynier